



Article

Oxygen and Sulfur Isotope Systematics of Dissolved Sulfate in a Nonvolcanic Geothermal System: Sulfate Source, Evolution and Impact on Geothermometers

Yinlei Hao ^{1,2} , Zhonghe Pang ^{3,*} , Qinghua Gong ², Nianqing Li ², Dawei Liao ⁴ and Zhengyu Luo ¹

¹ Key Laboratory of Synergetic Control and Joint Remediation for Soil & Water Pollution, Ministry of Ecology and Environment, Chengdu 610059, China; haoyl@gdas.ac.cn (Y.H.); luozhengyu15@cdut.edu.cn (Z.L.)

² Guangdong Geological Disaster Emergency Technology Research Center, Guangzhou Institute of Geography, Guangdong Academy of Sciences, Guangzhou 510070, China; gongqh1@gdas.ac.cn (Q.G.); 13975834916@163.com (N.L.)

³ State Key Laboratory of Lithospheric and Environmental Coevolution, Institute of Geology and Geophysics, Chinese Academy of Sciences, Beijing 100029, China

⁴ Sinopec Petroleum Exploration and Development Research Institute, Beijing 102206, China; ldw.syky@sinopec.com

* Correspondence: z.pang@mail.iggcas.ac.cn

Abstract: Dual isotopes of sulfate ($\delta^{34}\text{S}_{\text{SO}_4}$ and $\delta^{18}\text{O}_{\text{SO}_4}$), along with isotopes in water and trace elements of geothermal waters, are systematically investigated to quantitatively elucidate sulfate sources and oxygen and sulfur isotopic behaviors during deep groundwater circulation and to constrain reservoir temperatures in the Jimo nonvolcanic geothermal system on the eastern coast of China. The results show that $\delta^{34}\text{S}_{\text{SO}_4}$ and $\delta^{18}\text{O}_{\text{SO}_4}$ values in geothermal waters ranged from -21.0 to 5.7‰ and from 1.1 to 8.8‰ , respectively. An increase in SO_4 concentrations ($140\text{--}796$ mg/L) with a systematic decrease in $\delta^{34}\text{S}_{\text{SO}_4}$ and $\delta^{18}\text{O}_{\text{SO}_4}$ values was observed along the flow path from the central to eastern and western parts. The sulfate in the Middle Group was predominantly from atmospheric deposition, with sulfide oxidation contributions of $<27\%$. In contrast, $80\text{--}85\%$ of SO_4 in the Eastern Group is derived from pyrite oxidation. In the Western Group, the oxidation of multiple metal sulfides contributed $43\text{--}66\%$ of SO_4 . Sulfate oxidation and mixing of shallow groundwater caused reservoir temperatures to be underestimated by $9 \pm 6\text{--}14 \pm 16\%$ using silica and K-Mg geothermometers but overestimated by up to $52\text{--}62\%$ using sulfate–water oxygen isotope geothermometers. The estimated average target reservoir temperature was 144 ± 8 °C, with geothermal waters circulating to depths of $3.6\text{--}4.6$ km. This study offers new insights into the significant impact of sulfate-related processes on geothermometric estimates, a factor often overlooked when using aqueous geothermometers. It also provides valuable guidance for accurately estimating target geothermal reservoir temperatures and advancing exploration in nonvolcanic geothermal systems.

Keywords: sulfur isotope; oxygen isotope; geothermal system; sulfate source; sulfide oxidation; geothermometer



Academic Editor: José Manuel Marques

Received: 19 December 2024

Revised: 13 February 2025

Accepted: 6 March 2025

Published: 9 March 2025

Citation: Hao, Y.; Pang, Z.; Gong, Q.; Li, N.; Liao, D.; Luo, Z. Oxygen and Sulfur Isotope Systematics of Dissolved Sulfate in a Nonvolcanic Geothermal System: Sulfate Source, Evolution and Impact on Geothermometers. *Water* **2025**, *17*, 788. <https://doi.org/10.3390/w17060788>

Copyright: © 2025 by the authors. Licensee MDPI, Basel, Switzerland. This article is an open access article distributed under the terms and conditions of the Creative Commons Attribution (CC BY) license (<https://creativecommons.org/licenses/by/4.0/>).

1. Introduction

Hydrochemical and isotope investigations of geothermal fluids are among the most economical and effective tools for geothermal exploration and development and utilization and can reflect thermal conditions at depth and provide critical information on the origin of geothermal fluids, subsurface flow direction and subsurface temperatures [1–5]. Estimating the target geothermal reservoir temperatures based on the chemical and isotopic

compositions of geothermal water is one of the first steps in determining the potential use of a particular geothermal reservoir [1,6,7]. A wide variety of effective geothermometers, including chemical geothermometers (e.g., silica, Na-K, Na-K-Ca, K-Mg, Na-K-Mg and Na-Li), isotopic geothermometers (e.g., sulfate–water oxygen isotope geothermometer ($^{18}\text{O}(\text{SO}_4\text{-H}_2\text{O})$) and geothermometric modeling based on the chemical compositions of geothermal fluids, have been developed since the mid-1960s [6–18]. When applying these geothermometers, a principal assumption is always made that chemical and isotopic equilibrium between water and minerals is achieved in the source aquifer and cannot be significantly modified by secondary processes as the water ascends to the point of sampling [1,19]. However, this assumption is not necessarily true for all areas, especially where shallow secondary processes such as mixing re-equilibrium [20,21], mineral precipitation/dissolution reactions and degasification [7,17] are universal. In this case, the species concentrations and isotopic compositions can be altered, resulting in an apparent temperature discordant with the actual reservoir temperature [7,13]. Therefore, prior to estimating geothermal reservoir temperatures, it is necessary to acquire a sound understanding of the geochemical evolution of geothermal fluids and evaluate the impact of these processes on geothermometers, which is crucial for the sustainable use of geothermal water resources.

The Jimo geothermal system is located in the southeastern Jiaodong Peninsula, which is an important sector of the eastern coast of China, with abundant low- to medium-temperature geothermal resources [22–24]. Previous research based on the analysis of nonreactive elements (e.g., B and Cl), boron isotope ($\delta^{11}\text{B}$) and strontium isotope ($^{87}\text{Sr}/^{86}\text{Sr}$) has suggested that high salinity observed in the study area (up to 10.8 g/L) results from the dissolution of marine evaporites and minor seawater mixing [23]. However, the significant variations in SO_4 concentrations and trace metal element concentrations across the western, central and eastern parts of a specific 0.2 km² area remain poorly understood. These variations, particularly regarding the sources and evolution of sulfate, cannot be fully explained by the previously proposed mechanisms for salinity. This also prevents the use of geochemical geothermometers to determine the proper geothermal reservoir temperature.

Sulfur and oxygen isotopes of sulfate ($\delta^{34}\text{S}_{\text{SO}_4}$ and $\delta^{18}\text{O}_{\text{SO}_4}$) have been proven to be robust tools for elucidating the evolution of sulfate in volcanic and nonvolcanic geothermal fluids [2,25–27]. The distinct $\delta^{34}\text{S}_{\text{SO}_4}$ and $\delta^{18}\text{O}_{\text{SO}_4}$ of dissolved sulfate derived from various sources, e.g., atmospheric deposition, seawater, evaporites, sulfide oxidation and magmatic degassing, may reveal sulfate origins in natural waters [2,26,28–34]. Furthermore, the original sulfur and oxygen isotope signals of sulfate are easily modified by secondary abiotic and biological processes, including sulfate reduction [35,36], disproportionation of magmatic SO_2 to H_2S and SO_4 [25] and oxygen isotope exchange between sulfate and water [37,38], that can be identified by the trend of the evolution in $\delta^{34}\text{S}_{\text{SO}_4}$ values, $\delta^{18}\text{O}_{\text{SO}_4}$ values and SO_4 concentrations.

Here, we combine new data on $\delta^{34}\text{S}_{\text{SO}_4}$ and $\delta^{18}\text{O}_{\text{SO}_4}$ values as well as trace elements in geothermal waters and shallow groundwaters with previously reported data on major ions (i.e., Na, K, Mg, Ca, HCO_3 , SO_4 and Cl) to elucidate sulfate sources and geochemical processes related to the evolution of sulfate concentrations and sulfur and oxygen isotopes of sulfate and to quantitatively assess the influence of these secondary processes on chemical geothermometers, including chemical (chalcedony, quartz, Na-K, Na-K-Ca, K-Mg and Na-Li) and sulfate–water oxygen isotope geothermometers. We determined the deep geothermal reservoir temperature based on proper geothermometers. The Jimo geothermal system can serve as a model system for the quantitative identification of shallow secondary processes, especially sulfate-related processes, and for the assessment of their impact on aqueous geothermometers.

2. Geologic Setting

The Jimo geothermal system is located in the southeastern Jiaodong Peninsula in China, which neighbors the Yellow Sea in the east (Figure 1). Tectonically, the study area is situated in the Mouping–Jimo fault zone, which is an important part of the giant Tanlu strike–slip fault system, and forms the boundary between the North China Block and the Sulu orogenic belt [39] (Figure 1a). The Jimo geothermal field is located at the junction of the NE-trending Wenquan–Cangkou fault and the NW-trending Dongkuang–Shuibao fault (Figure 1b). The primary NE-trending Wenquan–Cangkou fault is a tensional fault at an early stage and a compressional fault at a later stage and provides a suitable geothermal pathway [40]. The NW extensional fault is a small-scale water-conducting fault. The dominant strata are Early Cretaceous Laiyang Group clastic rocks (K_1l) and Qingshan Group (K_1q) pyroclastic rocks. The Laiyang Group is a fluvial–lacustrine sedimentary sequence that includes sandstone, conglomerate and mudstone. The Qingshan Group consists of intermediate-acid and intermediate-basic volcanic rocks [23,41–43] (Figure 1b). Quaternary unconsolidated sediments are widely distributed in geothermal fields at depths of 10–25 m and consist of Holocene black marine mud, brown lagoon clay and lacustrine silty sediment from bottom to top [40]. Magmatic activity was intense during the Early Cretaceous, with widespread intrusive rocks such as granite, andesite, quartz monzonite and adamellite. Geothermal wells with depths ranging from 125 to 394 m are distributed at the junction of the NE and NW faults, with an area of 0.2 km² (Figure 1c). The maximum yield of a single well reaches 1019 m³/d. The lithology of the geothermal reservoir is dominated by Early Cretaceous Laiyang Group sandstone. The geothermal waters are rich in Br, K, Ca, Mg, I, Ra and Rn, with a content of 58.1 Bq/L, and are used for spas and baths [44,45].

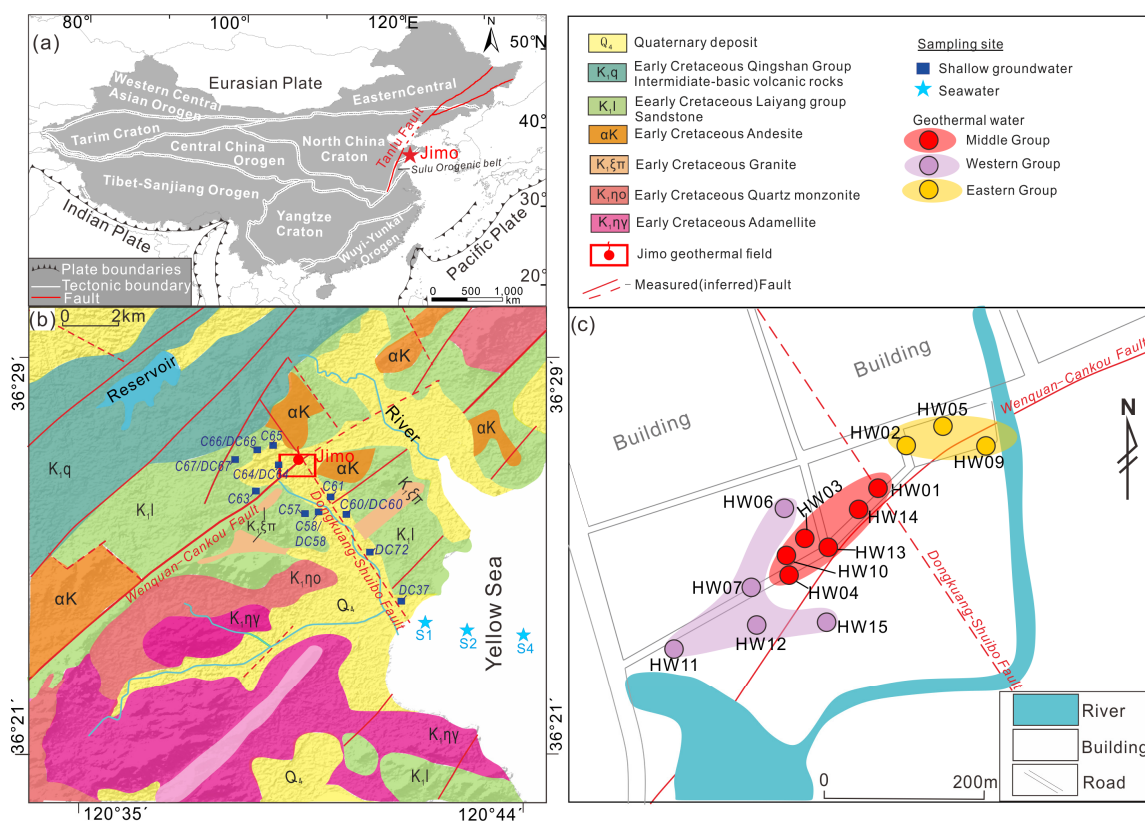


Figure 1. (a) The tectonic location of the Jimo geothermal system; major tectonic units in China, modified from [46]. (b) Lithologies and tectonics of the study area and sampling sites of shallow groundwater and seawater [23,43]. (c) Sampling locations of geothermal water.

3. Materials and Methods

3.1. Sampling and Laboratory Analysis

Geological field campaigns and sample collections were conducted in July and November 2017. Fourteen geothermal waters were sampled from geothermal wells at depths of 120 to 200 m. Sixteen additional shallow cold groundwaters were sampled from wells at depths of 10–40 m and three seawater samples were collected from the Yellow Sea at a depth of 1–1.5 m (Figure 1b). Sampling from geothermal wells and cold groundwater wells was performed after continuous pumping of the wells for more than 20 min. The temperature, pH, electrical conductivity (EC) and electromotive potential (Eh) were measured at the site with a portable multiparameter (HQ40D, Hach). The portable multiparameter was calibrated to a standard solution at 25 °C before sampling. Total alkalinity was titrated with a digital titrator (16900, Hach, Loveland, CO, USA) with 0.16 N sulfuric acid. All water samples were filtered at the site using a 0.45 µm syringe filter before the storage of water in HDPE bottles sealed with parafilm. Samples for major cation and trace element analysis were acidified to pH < 2 using 6 N redistilled HNO₃. Once collected, all the samples were stored at 4 °C for geochemical and isotope analysis within 3 months.

Major cations (K, Na, Ca and Mg) were analyzed with inductively coupled plasma optical emission spectroscopy (ICP–OES). Trace elements (e.g., Sr, Al, Fe, Mn, Mo, Zn, Tl and Pb) were analyzed with inductively coupled plasma–mass spectrometry (ICP–MS). The analytical precisions for major ions and trace elements were less than 0.5%. Major anions (Cl, SO₄ and NO₃) were analyzed with a DIONEX-500 ion chromatograph with a detection limit of 0.05 mg/L [23]. The oxygen isotopic compositions of water ($\delta^{18}\text{O}_{\text{H}_2\text{O}}$) were measured in the Water–Rock Interaction Laboratory, Institute of Geology and Geophysics, Chinese Academy of Sciences (IGG-CAS) using a laser absorption water isotope spectrometer analyzer (Picarro L 1102-i). Calibration was performed using three reference materials: GBW04458 ($\delta^{18}\text{O} = -0.15\text{‰}$), GBW04459 ($\delta^{18}\text{O} = -8.61\text{‰}$) and GBW04460 ($\delta^{18}\text{O} = -19.13\text{‰}$). The precision (1σ) for $\delta^{18}\text{O}_{\text{H}_2\text{O}}$ was better than 0.1‰. The sulfur and oxygen isotopic composition of sulfate ($\delta^{34}\text{S}_{\text{SO}_4}$ and $\delta^{18}\text{O}_{\text{SO}_4}$) were determined at the Laboratory for Stable Isotope Geochemistry, IGG-CAS using a Flash 2000 HT elemental analyzer coupled to a Delta V Advantage isotope ratio mass spectrometer (Thermo Fisher Scientific, Waltham, MA, USA). Samples were prepared through acidification to pH < 3, boiling and precipitation of BaSO₄ by addition of BaCl₂ solution. The BaSO₄ was recovered by washing several times with deionized water and then oven-dried at 80 °C. The dried BaSO₄ was subsequently thermally decomposed in an elemental analyzer to produce SO₂ for $\delta^{34}\text{S}_{\text{SO}_4}$ analysis and in a pyrolysis reactor to generate CO for $\delta^{18}\text{O}_{\text{SO}_4}$ analysis [47]. For $\delta^{34}\text{S}_{\text{SO}_4}$, two international standards (NBS127 and IAEA-SO-5) were used for normalization. The $\delta^{18}\text{O}_{\text{SO}_4}$ was calibrated using two international standards (NBS127 and IAEA-601). The analytical uncertainties (1σ) were better than $\pm 0.3\text{‰}$ for $\delta^{34}\text{S}_{\text{SO}_4}$ and $\pm 0.3\text{‰}$ for $\delta^{18}\text{O}_{\text{SO}_4}$. The oxygen and sulfur isotope ratios are expressed as δ -notions as per mil (‰) ($\delta = (R_{\text{sample}}/R_{\text{standard}} - 1) \times 1000$) relative to the Vienna Standard Mean Ocean Water (V-SMOW) standard ($\delta^{18}\text{O}_{\text{H}_2\text{O}}$ and $\delta^{18}\text{O}_{\text{SO}_4}$) and to the Vienna Canyon Diablo Troilite (V-CDT) standard ($\delta^{34}\text{S}_{\text{SO}_4}$), respectively.

3.2. Interpretation Techniques

Geothermometric modeling is based on fundamental methods for calculating multicomponent chemical equilibria in aqueous systems [48]. During the modeling process, the chemical compositions of geothermal water are used to determine the temperature at which a set of minerals is in equilibrium with the geothermal water. This is achieved by plotting $\log(Q/K)$ versus temperature for various minerals. The average equilibrium temperature of the minerals can be regarded as the best estimate of the subsurface temper-

ature. Geothermometric modeling in this study was conducted using the SOLVEQ-XPT program, along with the SOLTHERM-XPT data file [49]. This program allows for computing aqueous–mineral–gas equilibria at any specified pressure up to 5 kbar and temperature up to 600 °C.

A partial correlation analysis was applied to evaluate the influence of secondary processes on geothermometers and to identify the most influential processes. Statistical analyses were performed using SPSS 25.0.

4. Results

4.1. Geochemical Characteristics of Geothermal Fluids

The chemical and isotopic results for geothermal water, shallow groundwater and seawater are shown in Tables 1 and 2. Major cations and anions of 14 geothermal waters, 12 shallow groundwaters and 3 seawaters from the previous study [23] are presented in Table S1. The geothermal water is dominated by Cl-Na-Ca and Cl-Na with high total dissolved solids (TDS) (2472–10,832 mg/L) and significant variations in the concentrations of trace elements, e.g., Al (0.47–272 µg/L), Fe (<0.002–12,100 µg/L), Mn (80–3390 µg/L), Mo (1.4–67.7 µg/L), Zn (11.4–245 µg/L), Pb (0.03–133 µg/L), Tl (0.8–161 µg/L), Sr (6.5–52.8 mg/L) and Si (25.7–65.2 mg/L). The TDS and wellhead temperatures exhibited similar decreasing patterns from the central to the western and eastern parts (Figure 2a,b), consistent with the flow pattern for deep hot water that upwells from the middle area close to the junction of the NE-trending Wenquan–Cangkou fault and NW-trending Dongkuang–Shuibo fault and then flows to the west and east (Figure 1c). In contrast, the pH and Eh data indicate a gradual transition in the geothermal environment, from acidic and oxidizing conditions (pH = 4.2, Eh = 157.2 mV) in the eastern parts to weakly alkaline and reducing conditions (pH = 7.5, Eh = −44.6 mV) in the central and western parts (Figure 2c,d). Geothermal water samples were classified into three groups according to their geographical distribution, temperature and physicochemical characteristics: the Middle Group, Western Group and Eastern Group. The Middle Group samples were characterized by the highest TDS (6.7–10.8 g/L) and lowest SO₄ concentration (140–178 mg/L) and SO₄/Cl molar ratio (0.008–0.015) (Table 1). The Western Group samples exhibited lower TDS (2.5–5.1 g/L) but higher SO₄ (174–314 mg/L) and SO₄/Cl molar ratios (0.032–0.063) than the Middle Group samples. The Eastern Group samples exhibited the highest SO₄ concentration (603–796 mg/L) and SO₄/Cl molar ratio (0.057–0.069) with relatively constant TDS (7.2–8.1 g/L). Compared with geothermal waters, shallow groundwater samples had lower TDS (559–1118 mg/L), SO₄^{2−} (25.4–156 mg/L), Si (4.1–12.6 mg/L), Sr (0.56–2.2 mg/L) and Al (<0.002–1.25 µg/L) concentrations but higher SO₄/Cl molar ratios (0.23–1.27) (Table S1).

Table 1. Physical and chemical parameters and sulfur and oxygen isotopes of sulfate in geothermal waters, shallow groundwater and seawater.

| Sample ID | Water Type | Tem ^a °C | pH ^a | Eh ^a mV | TDS ^a mg/L | SO ₄ ^a mg/L | δ ¹⁸ O _{H₂O} ‰V-SMOW | δ ³⁴ S _{SO₄} ‰V-CDT | δ ¹⁸ O _{SO₄} ‰V-SMOW |
|-----------|------------|------------------------|-----------------|-----------------------|--------------------------|--------------------------------------|--|---|--|
| C63 | SG | 14.2 | 7.0 | −19.8 | 651 | 113 | −6.2 | 1.6 | 10.5 |
| C64 | SG | 18.2 | 7.7 | −64.4 | 661 | 25.4 | −6.9 | 3.7 | 8.8 |
| C66 | SG | 15.2 | 7.2 | −31.6 | 889 | 94.5 | −6.4 | 3.9 | 7.5 |
| S2 | SW | nd | 7.9 | −40.2 | 33,778 | 2316 | −0.2 | 19.7 | 10.0 |
| S3 | SW | nd | 8.0 | −49.3 | 33,731 | 2327 | −0.3 | 20.1 | 8.4 |
| HW01 | GW-M | 89.5 | 6.8 | −7.1 | 10,832 | 140 | −8.3 | 5.7 | 6.1 |
| HW03 | GW-M | 88.0 | 7.0 | −21.9 | 8961 | 178 | −8.3 | 0.6 | 7.6 |
| HW04 | GW-M | 80.0 | 6.9 | −16.4 | 6723 | 156 | −7.9 | −0.3 | 8.7 |

Table 1. Cont.

| Sample ID | Water Type | Tem ^a °C | pH ^a | Eh ^a mV | TDS ^a mg/L | SO ₄ ^a mg/L | δ ¹⁸ O _{H₂O} ‰V-SMOW | δ ³⁴ S _{SO₄} ‰V-CDT | δ ¹⁸ O _{SO₄} ‰V-SMOW |
|-----------|------------|---------------------|-----------------|--------------------|-----------------------|-----------------------------------|---|--|---|
| HW10 | GW-M | 86.0 | 6.7 | 1.3 | 6982 | 153 | −7.9 | nd | nd |
| HW13 | GW-M | 88.1 | 7.2 | −19.5 | 8600 | 162 | −8.2 | −0.0 | 8.8 |
| HW14 | GW-M | 86.7 | 7.1 | −9.0 | 10,462 | 158 | −8.4 | 1.1 | 8.4 |
| HW06 | GW-W | 74.3 | 7.2 | −30.5 | 2722 | 240 | −7.1 | −4.1 | 4.3 |
| HW07 | GW-W | 70.0 | 7.4 | −44.6 | 5077 | 247 | −7.2 | −4.5 | 6.2 |
| HW11 | GW-W | 60.0 | 7.3 | −39.6 | 2472 | 174 | −6.1 | nd | nd |
| HW12 | GW-W | 70.2 | 7.1 | −27.6 | 3609 | 299 | −6.6 | nd | nd |
| HW15 | GW-W | 48.2 | 7.5 | −18.3 | 4189 | 314 | −6.4 | −15.4 | 6.4 |
| HW02 | GW-E | 66.8 | 6.8 | −5.4 | 7182 | 603 | −7.5 | −14.0 | 3.5 |
| HW05 | GW-E | 66.9 | 6.7 | −1.7 | 7725 | 722 | −7.9 | −15.1 | 2.6 |
| HW09 | GW-E | 60.0 | 4.2 | 157.2 | 8057 | 796 | −7.9 | −21.0 | 1.1 |

Note(s): SG: shallow groundwater, SW: seawater, GW-M: Middle Group geothermal water, GW-W: Western Group geothermal water, GW-E: Eastern Group geothermal water, Tem: wellhead temperature. ^a Data from [23].

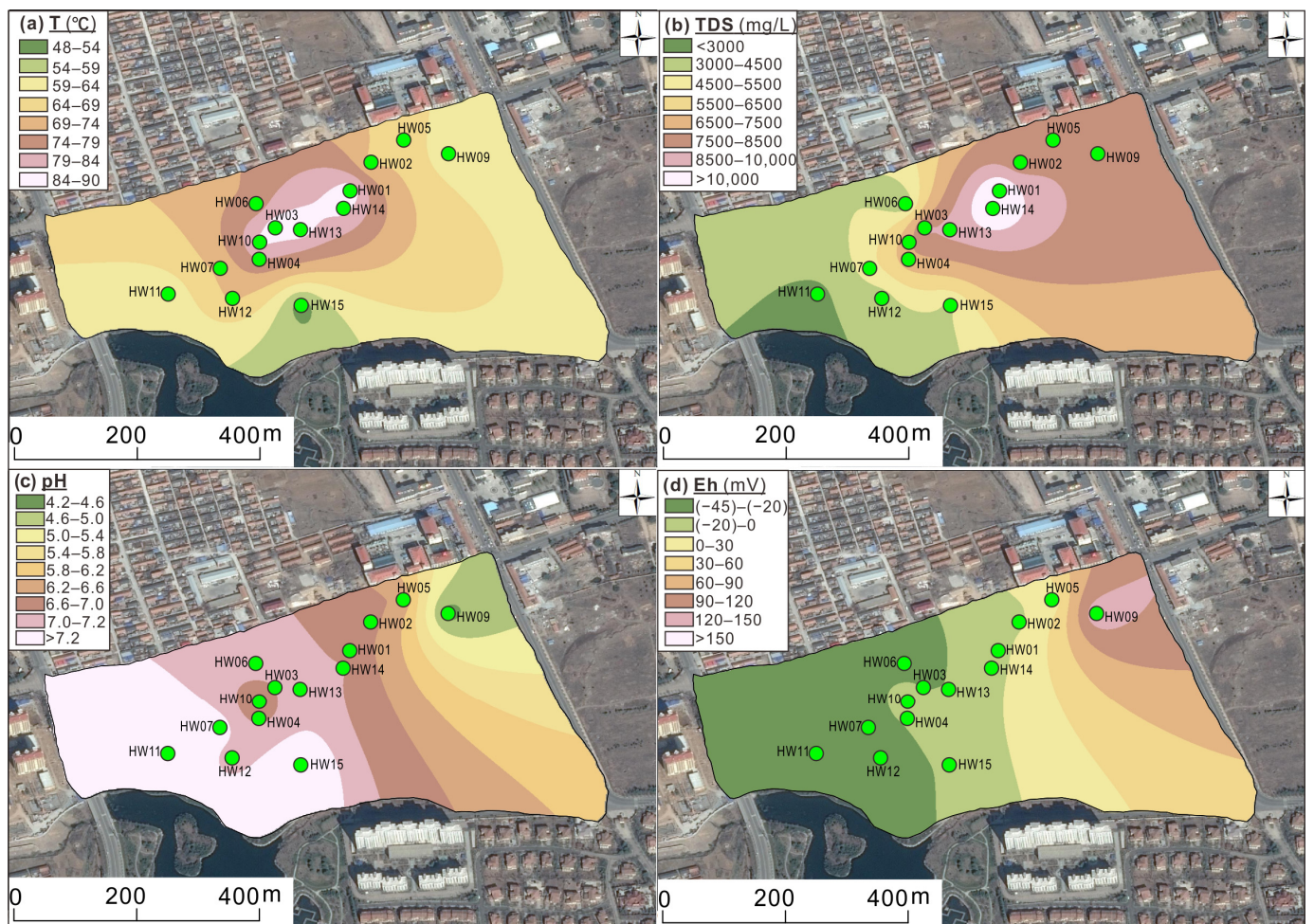


Figure 2. Spatial patterns of the wellhead temperature (T°C) (a), TDS (mg/L) (b), pH (c) and Eh (mV) for geothermal water (d).

Table 2. Trace elements in geothermal waters.

| Sample ID | Water Type | Si ^a mg/L | Sr ^a mg/L | Al ^a µg/L | Fe µg/L | Mn µg/L | Mo µg/L | Zn µg/L | Tl µg/L | Pb µg/L |
|-----------|------------|----------------------|----------------------|----------------------|---------|---------|---------|---------|---------|---------|
| HW01 | GW-M | 54.9 | 52.8 | 4.21 | 242 | 243 | 13.9 | 16.0 | 7.9 | 0.11 |
| HW03 | GW-M | 54.9 | 40.6 | 1.30 | 27 | 280 | 63.8 | 57.3 | 6.7 | 0.49 |
| HW04 | GW-M | 51.7 | 34.6 | 2.36 | 7 | 256 | 35.7 | 11.6 | 8.2 | 2.08 |
| HW10 | GW-M | 53.5 | 32.1 | 1.98 | 37 | 210 | 45.8 | 55.4 | 7.1 | 1.75 |
| HW13 | GW-M | 54.6 | 41.1 | 0.81 | 21 | 280 | 36.4 | 16.5 | 7.5 | 0.03 |
| HW14 | GW-M | 61.4 | 49.8 | 0.91 | 8 | 275 | 22.9 | 19.9 | 10.8 | 0.03 |
| HW06 | GW-W | 25.7 | 7.89 | 1.47 | 11 | 118 | 63.4 | 148 | 3.4 | 9.97 |
| HW07 | GW-W | 33.0 | 23.1 | 2.48 | 14 | 359 | 36.5 | 11.4 | 15.2 | 0.34 |
| HW11 | GW-W | 35.8 | 6.53 | 0.61 | 42 | 79.7 | 9.9 | 32.8 | 0.8 | 0.28 |
| HW12 | GW-W | 28.0 | 12.9 | 2.18 | 25 | 365 | 67.7 | 52.9 | 22.4 | 0.29 |
| HW15 | GW-W | 28.5 | 16.5 | 0.81 | 94 | 366 | 10.1 | 18.4 | 4.0 | 1.74 |
| HW02 | GW-E | 35.0 | 32.1 | 0.56 | 20 | 693 | 12.6 | 39.4 | 5.8 | 133 |
| HW05 | GW-E | 35.9 | 36.6 | 0.47 | <0.002 | 1280 | 10.7 | 51.7 | 19.4 | 80.6 |
| HW09 | GW-E | 65.2 | 34.8 | 272 | 12,100 | 3390 | 1.4 | 245 | 161 | 99.4 |

Note(s): ^a data from [23].

4.2. Sulfur and Oxygen Isotopes ($\delta^{18}O_{SO_4}$ and $\delta^{34}S_{SO_4}$) in Sulfate

The $\delta^{34}S_{SO_4}$ values for dissolved sulfate in geothermal waters varied from -21.0‰ to 5.7‰ , which were much lower than those of seawater (19.7 to 20.1‰) and overlapped with those of shallow groundwater (1.6 to 3.9‰) (Table 1). The $\delta^{34}S_{SO_4}$ values for dissolved sulfate in geothermal waters in the study area are also much lower than those in volcanic geothermal waters worldwide (-2.0‰ to $+24.7\text{‰}$ [3,50]) and in nonvolcanic geothermal waters, e.g., 26‰ to 30‰ for the Tangquan Karst geothermal system [26] and 3.17‰ to 17.89‰ for in Pearl River Delta region [2] in the east China region (Figure 3). The $\delta^{18}O_{SO_4}$ values for sulfate in geothermal waters ranged from 1.1‰ to 8.8‰ , which were lower than those of seawater (8.4 to 10.0‰) and shallow groundwater (7.5 to 10.5‰). Besides, in geothermal waters, the $\delta^{18}O_{SO_4}$ values for dissolved sulfate were 9 – 17‰ higher than the $\delta^{18}O_{H_2O}$ values for water (-8.4 to -6.1‰). The measured $\delta^{34}S_{SO_4}$ and $\delta^{18}O_{SO_4}$ for seawater sulfate around the Jimo geothermal systems were close to those of modern seawater sulfate ($\delta^{34}S_{SO_4} = 21.0 \pm 0.2\text{‰}$ [51], $\delta^{18}O_{SO_4} = 9.5\text{‰}$ [52]). The decreasing trends of the $\delta^{34}S_{SO_4}$ and $\delta^{18}O_{SO_4}$ values for the geothermal waters from the Middle Group to the Western Group and Eastern Group (Table 1) were consistent with those of the TDS and temperature, while they contrasted with the increasing trend of the SO_4 concentration.

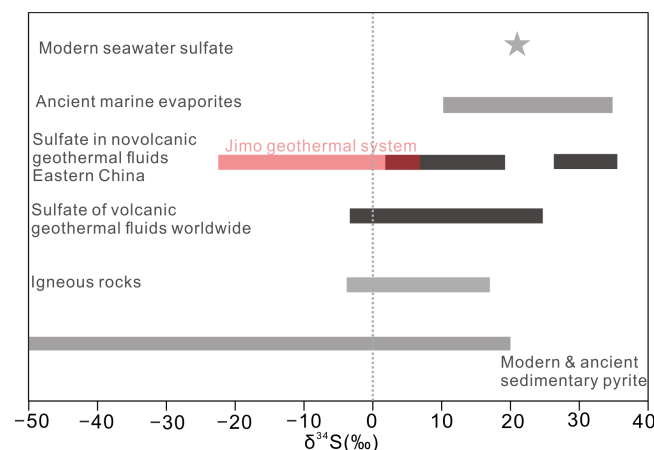


Figure 3. Comparison of $\delta^{34}S$ values for sulfate (red line) in Jimo geothermal water with those of sulfides and sulfate in various geologic reservoirs. The $\delta^{34}S$ values for sulfides of igneous rocks and

modern and ancient sediments, and sulfate of ancient marine evaporites are shown as gray lines [29,30,51,53,54]. The black lines indicate previously reported $\delta^{34}\text{S}$ values for dissolved sulfate in volcanic geothermal water worldwide [25,50,55,56] and nonvolcanic geothermal water in east China [2,26]. The star symbol represents the $\delta^{34}\text{S}$ value for dissolved sulfate in modern seawater.

5. Discussion

5.1. Geochemical Evolution of Geothermal Water

The geochemical variations in the Middle Group, Western Group and Eastern Group samples indicate that processes occurred along the flow pathway (Figure 4). Sample HW01 in the Middle Group is located at the cross-section of faults with the highest TDS and temperature and can be regarded as a deep-sourced fluid compared with the other samples. The significant increases in the concentrations of metal elements such as Fe, Mn, Zn, Pb and Tl, especially Fe, in HW09 were 50 times higher than those in HW01. This was accompanied by a much lower pH and higher Eh, SO_4 concentration and SO_4/Cl ratio, suggesting that the excess sulfate in Eastern Group samples may have resulted from the oxidization of metal sulfides, predominantly pyrite oxidization [31]. Moreover, the acidic environment further accelerated silicate and carbonate dissolution, as indicated by the synchronous increases in Al/Cl, Si/Cl, Ca/Cl and Mg/Cl.

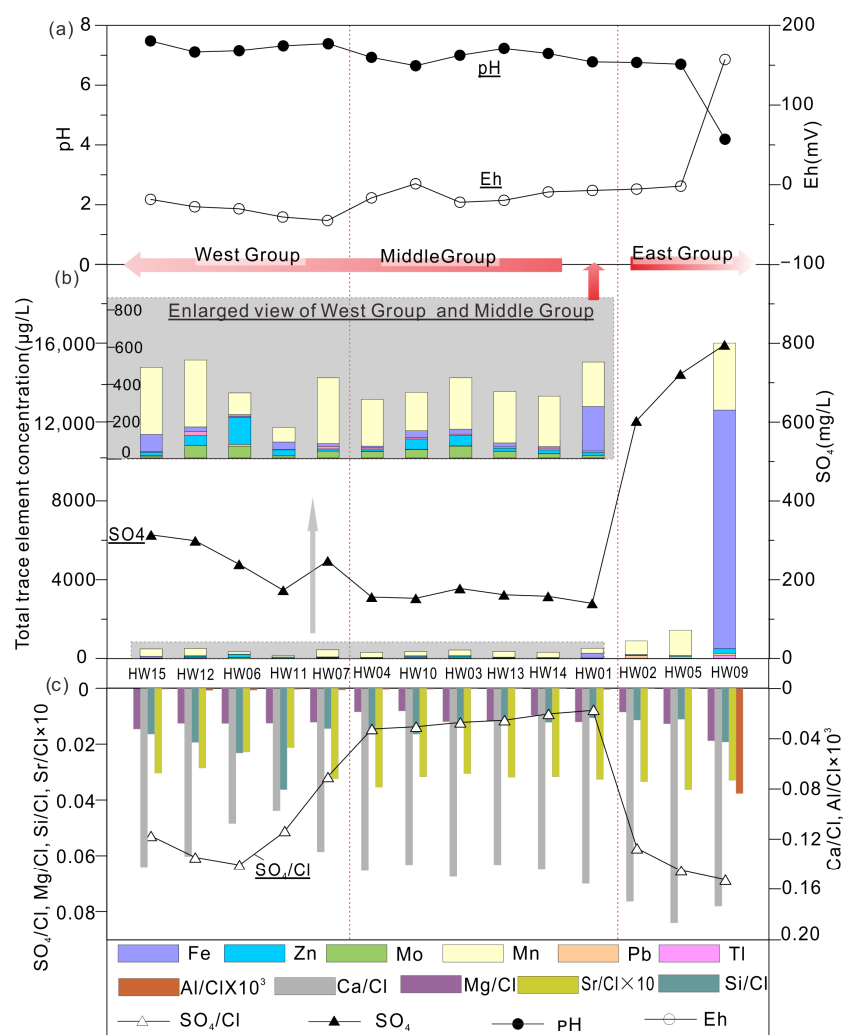


Figure 4. Hydrochemical characteristics and distribution of geothermal water in the Jimo Basin, including (a) pH and Eh; (b) total trace element and SO_4^{2-} concentrations; and (c) Sr/Cl, Si/Cl, Al/Cl, Ca/Cl, Mg/Cl and SO_4/Cl molar ratios.

In contrast to the SO_4 concentrations in the Middle Group samples, those in the Western Group samples slightly increased with increasing pH. The slight increases in the concentrations of Zn, Mn, Mo and Tl compared with those in HW01 indicated that oxidization of assemblages of metal sulfides (ZnS , MnS , MnS_2 , MoS_2) also occurred. Unlike in HW09, which is dominated by pyrite oxidization, the multimetal oxidization effect is relatively weaker and might be partially covered by mixing of shallow groundwater, as indicated by the lowest TDS and Cl concentrations and temperatures among the three groups. The significant increase in SO_4/Cl ratios with a slight increase in SO_4 for the Western Group samples could be the result of the compatible effect of mixing and metal sulfide oxidization. The lower variations in SO_4 , pH, temperature and SO_4/Cl for the Middle Group samples indicate the lower influence of shallow secondary processes, but a tiny fraction of metal-sulfide oxidization cannot be ruled out due to the difference in trace metal elements, such as the increase in Zn, Mn and Mo, compared with those in HW01.

5.2. Sources of Sulfate Constrained by Sulfur and Oxygen Isotope Systematics

Sulfate derived from natural sources, including sulfide oxidation, gypsum dissolution, soil sulfate and atmospheric deposition, exhibits different $\delta^{18}\text{O}_{\text{SO}_4}$ and $\delta^{34}\text{S}_{\text{SO}_4}$ values (Figure 5, [28,36]). Physical and biogeochemical processes, including the mixing of potential sources with different isotopic compositions, bacterial sulfate reduction and oxygen isotope exchange between sulfate and water, cause the evolutions of $\delta^{18}\text{O}_{\text{SO}_4}$ and $\delta^{34}\text{S}_{\text{SO}_4}$ values to have different trends (Figure 5a). The diagram of $\delta^{34}\text{S}_{\text{SO}_4}$ vs. $\delta^{18}\text{O}_{\text{SO}_4}$, combined with the lithology of the geothermal reservoirs (e.g., sandstone with overlying Quaternary sediments) and the recharge sources of geothermal water in the study area, was used to constrain the dominant sulfate sources in Jimo geothermal waters.

The plot of $\delta^{34}\text{S}_{\text{SO}_4}$ vs. $\delta^{18}\text{O}_{\text{SO}_4}$ shows that sulfate in shallow groundwater samples derives from atmospheric deposition. The sulfate in Middle Group geothermal water samples also originates from atmospheric deposition, but it is much older than that in shallow groundwater. This is supported by the geothermal water samples plotted on the local meteoric water line in the $\delta^{18}\text{O}_{\text{H}_2\text{O}}-\delta^2\text{H}_{\text{H}_2\text{O}}$ diagram, depleted in ^2H and ^{18}O relative to shallow groundwater, and by the ^{14}C age of geothermal water ($\sim 10,010$ years; ^{14}C : 17.40 pMC), which is older than that of shallow groundwater (~ 2500 years; ^{14}C : 72.5 pMC) [23]. Thus sulfur-containing atmospheric deposits with high $\delta^{34}\text{S}_{\text{SO}_4}$ values are carried by paleometeoric water into the deep geothermal reservoirs. The $\delta^{34}\text{S}_{\text{SO}_4}$ and $\delta^{18}\text{O}_{\text{SO}_4}$ values for sulfates in Eastern Group geothermal water samples are comparable to those of sulfate derived from the oxidation of reduced inorganic sulfide. This is additionally confirmed by the typical characteristics of sulfide oxidation, i.e., increases in SO_4 concentrations and SO_4/Cl ratios with decreases in $\delta^{34}\text{S}_{\text{SO}_4}$ and $\delta^{18}\text{O}_{\text{SO}_4}$ (Figure 6). Combined with the evidence from the major and trace elements shown in Section 5.1, the sulfide is dominated by pyrite. The $\delta^{18}\text{O}$ of sulfate formed by pyrite oxidation depends on oxidation processes; more specifically, this process involves the incorporation of oxygen atoms dominated by oxygen molecules ($\delta^{18}\text{O}_{\text{O}_2} = 23.8\%$, Equation (1)) or water molecules (generally depleted ^{18}O , Equation (2)) [36,57–59]. In reaction (1), 87.5% of the sulfate oxygen is derived from oxygen molecules and the remaining 12.5% is derived from water molecules, which yielded a relatively ^{18}O -rich sulfate. In reaction (2), 100% of the oxygen in sulfate is contributed by water molecules, and sulfate is depleted of ^{18}O [31]. In addition, the process of pyrite oxidation by ferric (Fe^{3+}) iron adds more moles of H^+ for each mole of pyrite oxidized and causes a lower pH compared with that of reaction (1) [60].

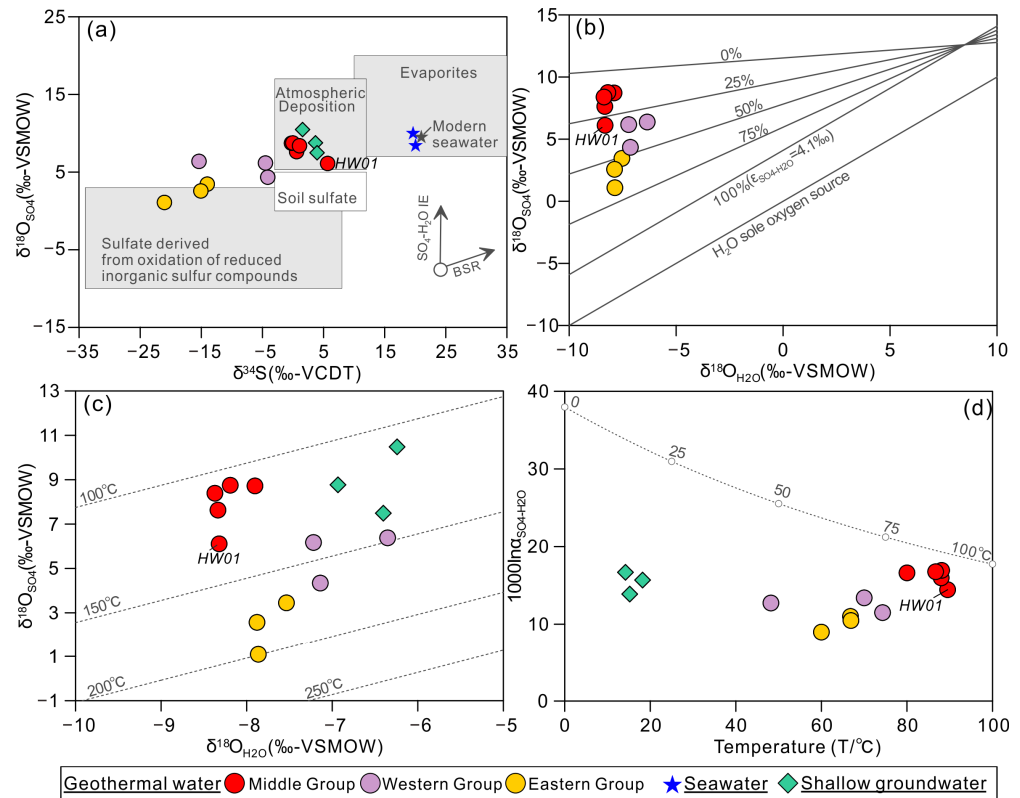
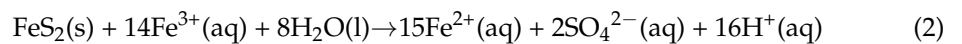
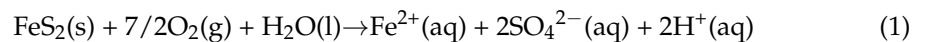


Figure 5. (a) Plot of $\delta^{34}\text{S}_{\text{SO}_4}$ vs. $\delta^{18}\text{O}_{\text{SO}_4}$ for sulfate in Jimo geothermal waters, shallow groundwater and seawater. Endmembers of atmospheric deposition, soil, seawater, evaporites and oxidation of reduced inorganic sulfur compounds are shown for reference [28,51,52]. Secondary processes include (1) bacterial sulfate reduction (BSR) and (2) oxygen isotope exchange between SO_4 and H_2O (SO_4 - H_2O IE). BSR causes isotope fractionation, enriching $\delta^{18}\text{O}_{\text{SO}_4}$ and $\delta^{34}\text{S}_{\text{SO}_4}$ in the residual sulfate with the ratio of 1:4 [35,36]. Plots of $\delta^{18}\text{O}_{\text{SO}_4}$ vs. $\delta^{18}\text{O}_{\text{H}_2\text{O}}$, (b–d) $10^3 \ln \alpha_{\text{SO}_4\text{-H}_2\text{O}}$ vs. wellhead temperature. The evolution of $\delta^{18}\text{O}_{\text{SO}_4}$, $\delta^{18}\text{O}_{\text{H}_2\text{O}}$ and $10^3 \ln \alpha_{\text{SO}_4\text{-H}_2\text{O}}$ with temperature is based on $10^3 \ln \alpha = 3.251 \times 10^6 / T^2 - 5.6$ [16].



To determine the predominant oxidation pathway of pyrite, the relative percentages of oxygen in sulfate incorporated by atmospheric O_2 and water were quantified using the $\delta^{18}\text{O}_{\text{SO}_4}$ for sulfate and the $\delta^{18}\text{O}_{\text{H}_2\text{O}}$ values for water based on the stable isotope mass balance (Equation (3), [31,61]).

$$\delta^{18}\text{O}_{\text{SO}_4} = f \times (\delta^{18}\text{O}_{\text{H}_2\text{O}} + \varepsilon_{\text{SO}_4\text{-H}_2\text{O}}) + (1-f) \times [0.875 \times (\delta^{18}\text{O}_{\text{O}_2} + \varepsilon_{\text{SO}_4\text{-O}_2}) + 0.125 \times (\delta^{18}\text{O}_{\text{H}_2\text{O}} + \varepsilon_{\text{SO}_4\text{-H}_2\text{O}})] \quad (3)$$

where f is the fraction of water-derived oxygen in sulfate through Equation (2), and $(1-f)$ represents the fraction of oxygen in sulfate derived from atmospheric oxygen and water through Equation (1).

Notably, $\varepsilon_{\text{SO}_4\text{-H}_2\text{O}}$ (+4.1‰) and $\varepsilon_{\text{SO}_4\text{-O}_2}$ (−11.2‰) are the isotopic enrichment factors for the incorporation of oxygen from water and atmospheric oxygen, respectively [57,62]. The oxygen mass balance suggests that the process of pyrite oxidation by ferric iron (Equation (2)) contributed to 51–66% of the oxygen in sulfate in Eastern Group geothermal waters (Figure 5b). Geothermal waters containing a greater percentage of water-derived oxygen in SO_4 are expected to have a lower pH since the H^+ produced from the process of pyrite oxidation by ferric iron is much greater than that produced by atmospheric oxygen

(Equation (1)), which was further confirmed by the lowest pH of 4 observed in HW09, which has the highest SO_4/Cl molar ratio (0.069) (Figure 4).

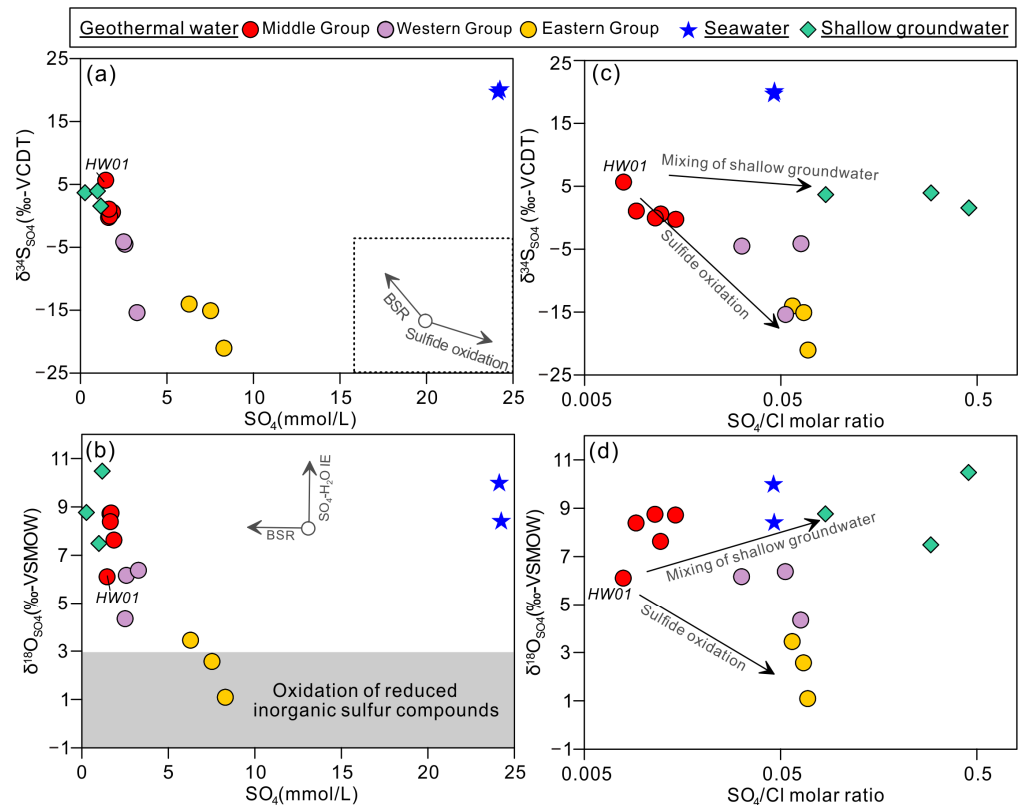


Figure 6. Plots of (a) $\delta^{34}\text{S}_{\text{SO}_4}$ vs. SO_4 (mmol/L), (b) $\delta^{18}\text{O}_{\text{SO}_4}$ vs. SO_4 (mmol/L), (c) $\delta^{34}\text{S}_{\text{SO}_4}$ vs. SO_4/Cl and (d) $\delta^{18}\text{O}_{\text{SO}_4}$ vs. SO_4/Cl for the Jimo geothermal waters. BSR: bacterial sulfate reduction, $\text{SO}_4\text{-H}_2\text{O}$ IE: oxygen isotope exchange between SO_4 and H_2O .

Western Group geothermal waters exhibit large variations in $\delta^{34}\text{S}_{\text{SO}_4}$ values and relatively constant $\delta^{18}\text{O}_{\text{SO}_4}$ values (Figure 5). This cannot be explained by a dominant single source (e.g., atmospheric precipitation or oxidation of sulfide minerals) or the influence of bacterial sulfate reduction, which generally results in a 1:4 kinetic relationship between the $\delta^{18}\text{O}_{\text{SO}_4}$ and $\delta^{34}\text{S}_{\text{SO}_4}$ of sulfate [35,36]. The $\delta^{34}\text{S}_{\text{SO}_4}$ - $\delta^{18}\text{O}_{\text{SO}_4}$ - SO_4 - SO_4/Cl relationship suggests both the influence of sulfide oxidation and mixing of shallow groundwater with low SO_4^{2-} concentrations but higher $\delta^{34}\text{S}_{\text{SO}_4}$ values and SO_4/Cl ratios (Figure 6), which is consistent with the explanation of geochemical characteristics in Section 5.1. Due to the involvement of multiple metal sulfides and the significant influence of shallow groundwater, it is challenging to identify sulfide oxidation pathways.

The exchange of oxygen isotopes between sulfate and water may also add a degree of uncertainty to the interpretation of $\delta^{18}\text{O}_{\text{SO}_4}$. The isotope exchange rate depends on the temperature and is inversely proportional to the pH of the aquifer water. Five hundred years is sufficient to reach 90% equilibrium at 100 °C at a pH of 7 [1]. Under the conditions of a deep reservoir, the pH, high temperature (>the highest measured wellhead temperature of 89.5 °C) and fluid residence time (about 10,010 years) are sufficient to achieve oxygen isotope exchange equilibrium between sulfate and water. However, the reservoir temperature is estimated to reach 198 °C for Eastern Group samples, which is 50 °C higher than that estimated for HW01 (Figure 5c). This suggests that the pyrite oxidation process disturbed the oxygen isotopic equilibrium between sulfate and water in the deep reservoir. In addition, the observed fractionation of oxygen isotopes between sulfate and water ($10^3 \ln \alpha_{\text{SO}_4\text{-H}_2\text{O}}$) in geothermal waters ranges from 9 to 17‰, which is lower than the

expected fractionation of 20–26‰ when oxygen isotope exchange equilibrium is achieved at a wellhead temperature of 48.2–89.5 °C (Figure 5d), especially for the Eastern Group and Western Group samples, suggesting that oxygen isotope re-equilibrium at shallow depth has not been achieved. Overall, sulfide oxidation at shallow depths disturbs the oxygen isotope exchange equilibrium between sulfate and water in deep reservoirs and is not completely masked by the shallow oxygen isotope exchange between sulfate and water.

5.3. Quantitative Contributions of Sulfate Sources and Sulfur Isotope of Sulfides

Dissolved sulfate in geothermal water originates from sulfide oxidation, mixing of shallow groundwater (atmospheric precipitation in ~2500 BP) and deep geothermal water represented by HW01 (atmospheric precipitation in the late Pleistocene), which can be quantified based on the mass balance of sulfate and chloride.

- (1) The proportion of solutes from shallow groundwater (x) in the mixing process of shallow groundwater and HW01 is determined based on the Cl mass balance model:

$$xn_{\text{Cl}(\text{SG})_{\text{Mea}}} + (1 - x)n_{\text{Cl}(\text{HW01})_{\text{Mea}}} = n_{\text{Cl}(\text{GW})_{\text{Mea}}} \quad (4)$$

- (2) The expected SO_4 concentrations formed by the mixing of shallow groundwater and HW01 are as follows:

$$xn_{\text{SO}_4(\text{SG})_{\text{Mea}}} + (1 - x)n_{\text{SO}_4(\text{HW01})_{\text{Mea}}} = n_{\text{SO}_4(\text{GW})_{\text{Cal}}} \quad (5)$$

- (3) The excess sulfate derived from sulfide oxidation:

$$\Delta n_{\text{SO}_4} = n_{\text{SO}_4(\text{GW})_{\text{Mea}}} - n_{\text{SO}_4(\text{GW})_{\text{Cal}}} \quad (6)$$

- (4) Contributions from different sources:

Sulfide oxidation:

$$Y_{\text{SO}} = \Delta n_{\text{SO}_4} / n_{\text{SO}_4(\text{GW})_{\text{Mea}}} \quad (7)$$

Shallow groundwater:

$$Y_{\text{SG}} = x(1 - Y_{\text{SO}}) \quad (8)$$

HW01:

$$Y_{\text{HW01}} = (1 - x)(1 - Y_{\text{SO}}) = 1 - Y_{\text{SO}} - Y_{\text{SG}} \quad (9)$$

where $n_{\text{SO}_4(\text{SG})}$ ($n_{\text{Cl}(\text{SG})}$), $n_{\text{SO}_4(\text{GW})}$ ($n_{\text{Cl}(\text{GW})}$) and $n_{\text{SO}_4(\text{HW01})}$ ($n_{\text{Cl}(\text{HW01})}$) refer to the concentration of SO_4^{2-} (Cl^-) in the shallow groundwater (SG), geothermal water except for HW01 (GW) and HW01; Δn_{SO_4} refers to the excess sulfate; and $_{\text{Mea}}$ and $_{\text{Cal}}$ represent the measured and calculated values, respectively. x is the proportion of solutes from shallow groundwater during the mixing process of shallow groundwater and HW01. Y_{SO} , Y_{SG} and Y_{HW01} are the proportions of sulfate from sulfide oxidation, shallow groundwater and HW01, respectively.

With an average SO_4 concentration of 0.94 ± 0.31 mmol/L and a Cl concentration of 3.25 ± 0.83 mmol/L for shallow groundwater (Figure 7), the results show that the sulfates of the Middle Group geothermal water samples are less affected by the mixing of shallow groundwater (0–31%) and sulfate oxidation (<27%) and are dominated by sulfate from HW01 (46–85%). In contrast, sulfide oxidation contributes significantly to the sulfate content in the Western Group and Eastern Group geothermal water samples. For the Western Group samples, the proportions of sulfate produced by sulfide oxidation range from 43 to 66%, with the contributions of shallow groundwater (23–47%) being greater than those of deep geothermal water (8–19%). For Eastern Group samples, sulfide oxidation contributes 80–85% of the total SO_4 , with higher proportions of sulfate from HW01 (10–12%) than from shallow groundwater (5–8%).

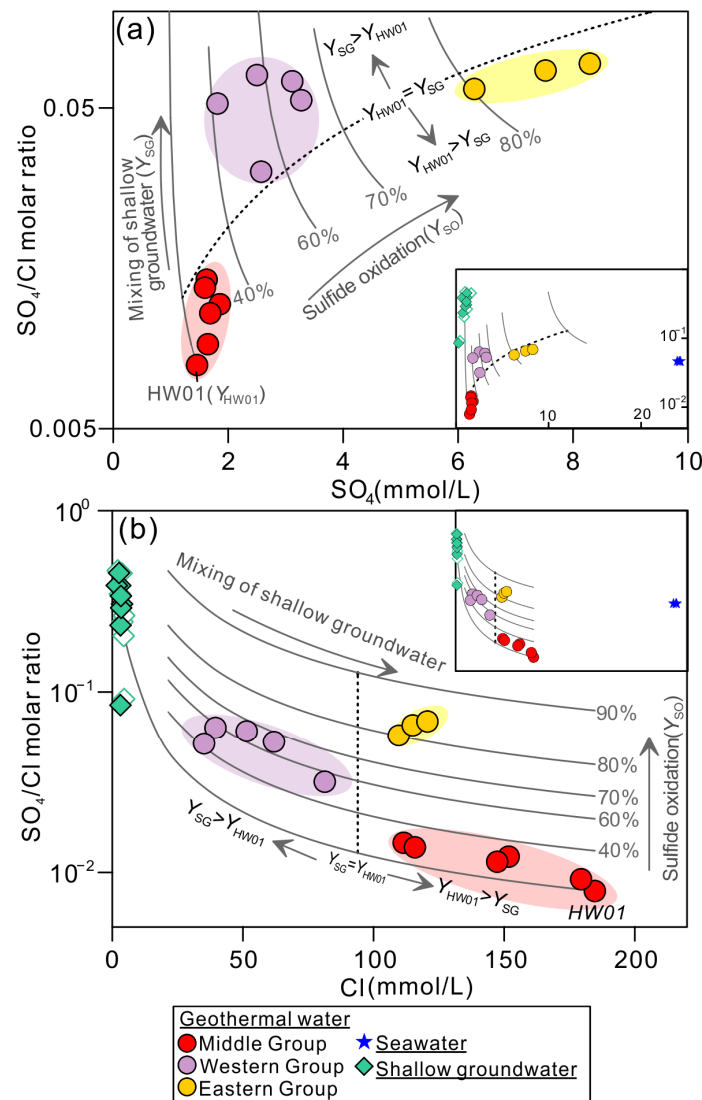


Figure 7. Plots of the SO₄/Cl molar ratio vs. SO₄ (a) and SO₄/Cl molar ratio vs. Cl (b) for the Jimo geothermal waters, shallow groundwater and seawater. The gray solid lines represent the proportions of sulfate in geothermal water derived from sulfide oxidation (Y_{SO}). The black dashed lines represent the proportions of sulfate from shallow groundwater relative to that from HW01 (Y_{SG}/Y_{HW01}).

Due to the lack of direct measurements of δ³⁴S values for sulfides in the study area, the δ³⁴S values for sulfides (R_{sulfide}) are calculated based on isotope mass balance using the δ³⁴S_{SO₄} values of shallow groundwater (R_{SG}), geothermal water (R_{GW}, excluding HW01) and HW01 (R_{HW01}) (Equation (10)). It was assumed that there is no discernible difference between δ³⁴S_{sulfide} in the parent sulfides and associated dissolved sulfate during the inorganic oxidation of sulfide (Δ_{SO₄-Sulfide} ≈ 0, [29,63]). The expected δ³⁴S values for sulfides range widely from −35.9‰ to −13.2‰ in the western area; however, the δ³⁴S values for pyrite in the eastern area are relatively constant, ranging from −29.5‰ to −21.9‰ (Figure 5). The inferred δ³⁴S values for sulfides are generally lower than those of igneous rocks but fall within the range of sedimentary sulfides from a variety of settings (Figure 3). Considering that Quaternary sediments, consisting of black marine mud, brown lagoon clay and lacustrine silty sediment, are widely distributed in the Jimo geothermal field at depths of 10–25 m [40], the sulfide minerals with inferred low δ³⁴S values are mostly likely to be derived from Quaternary sediments.

$$Y_{SO} \Delta n_{SO_4} R_{sulfide} + Y_{SG} n_{SO_4(SG)} R_{SG} + Y_{HW01} n_{SO_4(HW01)} R_{HW01} = n_{SO_4(GW)} R_{GW} \quad (10)$$

5.4. Impact on Geothermometers and Estimation of Geothermal Reservoir Temperature

5.4.1. Evaluation of the Influence of Secondary Processes on Different Geothermometers

Based on the geochemistry of geothermal waters, the temperatures of the Jimo geothermal reservoir have been estimated by 21 geothermometers, including silica geothermometers (chalcedony and quartz [8,10,64,65]), cation geothermometers (Na-K [12,13,64,66–68], Na-K-Ca [14], Na-K-Ca with Mg correction [9], K-Mg [13] and Na-Li [69,70], Li-Mg [71]) and sulfate–water oxygen isotope geothermometers [16,35,72] (Figure 8, Table S2). The temperatures estimated by different chalcedony and quartz geothermometers range from 104 ± 18 °C to 133 ± 17 °C (Table S3). The Mg-corrected Na–K–Ca geothermometer yielded a relatively lower temperature (147 ± 11 °C) than the Na–K–Ca geothermometer without correction (168 ± 11 °C). K-Mg geothermometers record a temperature of 115 ± 8 °C, which is similar to that of chalcedony. Sulfate–water oxygen isotope geothermometers yield temperatures ranging from 135 ± 34 °C to 142 ± 30 °C. The Na-K geothermometers yield much higher reservoir temperatures (156 ± 10 °C to 201 ± 8 °C) than the other geothermometers. The Na–K–Mg triangle diagram suggests that not all of the geothermal water has reached the equilibrium and is partially equilibrated and immature; thus, Na-K geothermometers are not applicable in low- to medium-temperature Jimo geothermal systems (Figure S1). In contrast, the reservoir temperatures estimated by the Na-Li (69 ± 9 – 79 ± 9 °C) and Li-Mg (90 ± 4 °C) geothermometers are even lower than the wellhead temperatures and thus are not applicable to the Jimo geothermal system. In addition to the abnormally high and low temperatures measured by the Na-K, Na-K-Ca without Mg correction, Li-Na and Li-Mg geothermometers, the other geothermometers yield reservoir temperatures ranging from 105 ± 19 to 147 ± 11 °C. However, temperatures estimated by the same geothermometer vary up to 50–100 °C among different samples, suggesting the influence of secondary processes.

The impacts of different secondary processes on quartz, chalcedony, Na-K-Ca, K-Mg and sulfate–water oxygen isotope geothermometers were evaluated using the partial correlation relationships between the geothermometer and sulfate contributions from sulfide oxidation (Y_{SO}), shallow groundwater (Y_{SG}) and HW01 (Y_{HW01}) (Table 3). The extent to which the reservoir temperatures estimated for the geothermal samples (T) deviated from those estimated by HW01 (T_{HW01}) was also assessed ($\Delta T = (T - T_{HW01})/T_{HW01}$ (%)) (Table S4). The partial correlation coefficient of the Y_{SG} and silica (chalcedony and quartz) geothermometers is -0.562 at a significance level of $p < 0.1$. The mixing of shallow groundwater may cause the deep reservoir temperature to be underestimated by 10 ± 12 – $14 \pm 15\%$ on average, with the largest deviations of 27–36% for the Western Group samples. In addition, the reservoir temperature is overestimated by 7–9% for HW09, suggesting that sulfate oxidation can play a dominant role in silica geothermometers when the pH is low enough to dissolve silicate. The K-Mg geothermometer is strongly affected by sulfate oxidation, with a partial correlation coefficient of -0.730 at a significance level of $p < 0.01$. Sulfate oxidation accelerates water–rock interactions by differential dissolution of rock minerals and precipitation of secondary minerals, destroying the original K^2/Mg by decreasing K^2/Mg . The K-Mg geothermometer is also influenced by the mixing of shallow groundwater due to a decrease in temperature, which causes unsaturated water with primary rock minerals and enhances the mineral dissolution rate and decreases the K^2/Mg ratio [1]. In general, the deep reservoir temperatures are underestimated by $9 \pm 6\%$ on average, with the largest deviation of 18% by the K-Mg geothermometer. The sulfate–water oxygen isotope geothermometer is sensitive to the environment and is significantly influenced by sulfide oxidation, other undetermined reasons and mixing of shallow groundwater, with partial correlation coefficients of $0.897\sim 0.899$ ($p < 0.01$), $-0.718\sim -0.730$ ($p < 0.05$) and $-0.623\sim -0.624$ ($p < 0.1$), respectively. Sulfide oxidation can lead to a higher reservoir temperature, as estimated

by sulfate–water oxygen isotope geothermometers, because the addition of oxygen from water to sulfate decreases the difference in $\delta^{18}\text{O}$ values between sulfate and H_2O . The undetermined factors lowering the predicted temperatures may be the exchange of oxygen isotopes between sulfate and water at lower temperatures at shallow depths. The temperatures estimated by the sulfate–water oxygen isotope geothermometer, on average, were overestimated by 10 ± 24 – $13 \pm 28\%$, especially for Eastern Group samples, which are significantly influenced by sulfate oxidation, for which the temperature can be abnormally overestimated by up to 52–62%. The influence of secondary processes on the Na-K-Ca geothermometer with Mg correction is not significant, as the partial correlation coefficient is less than 0.5 ($p > 0.1$), indicating that the reservoir temperature was underestimated by $6 \pm 7\%$ on average. Generally, the degree to which the estimated temperatures based on the geothermometers in the middle group deviated from those in the HW01 group is small, ranging from 0–6%, except for those estimated by the sulfate–water oxygen isotope geothermometer, which underestimated the reservoir temperature by 11–20% (Table S4).

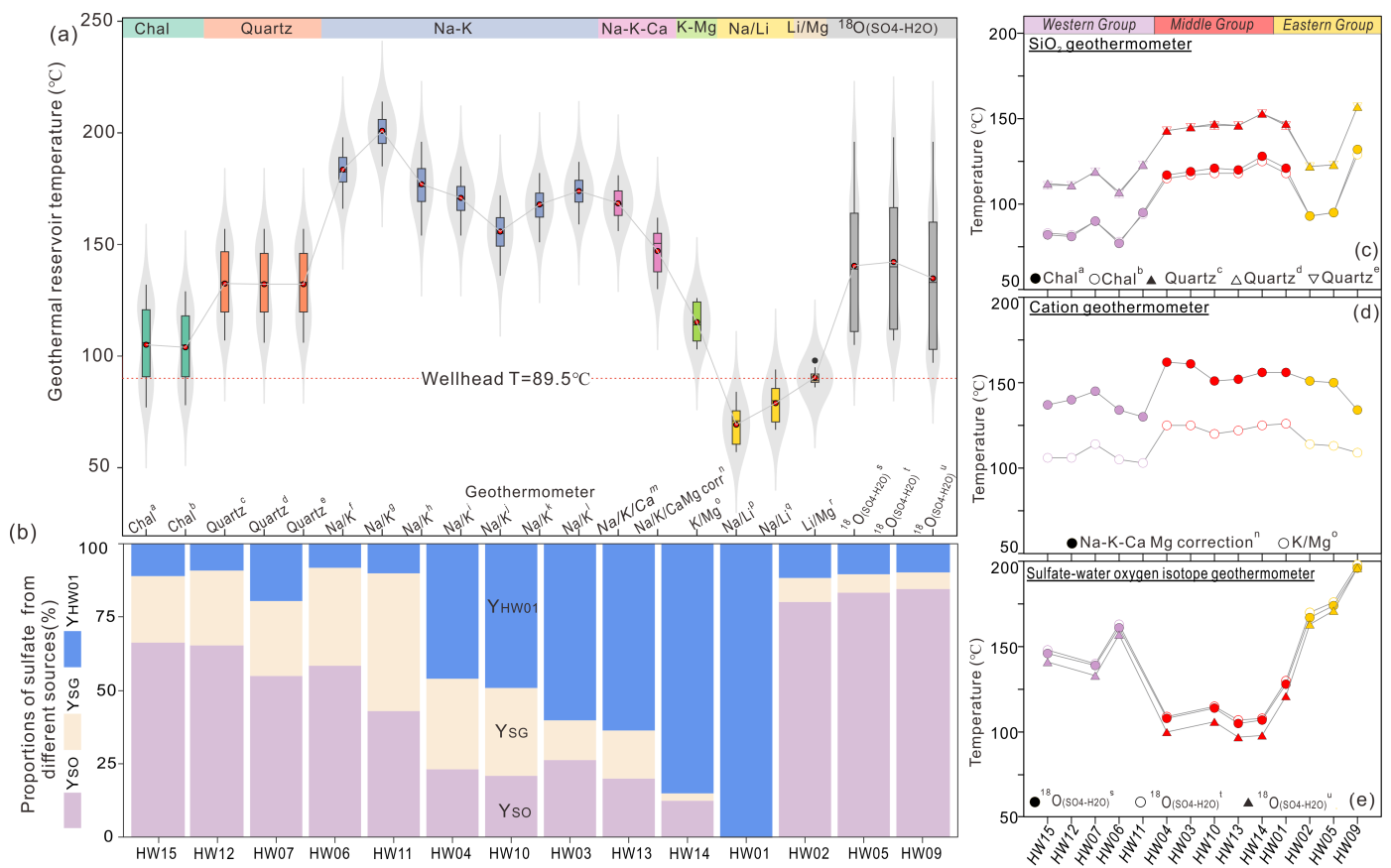


Figure 8. (a) Geothermal reservoir temperatures estimated by chalcedony and quartz geothermometers (a [8], b [64], c [10], d [8], e [65]), cation geothermometers (f [11], g [13], h [66], i [67], j [64], k [12], l [68], m [14], n [9], o [13], p [69], q [70]; r [71]) and sulfate–water oxygen isotope geothermometers (s [72], t [16], u [35]). The box plots and violin plots show the median, top and bottom quartiles. (b) Stacked bar chart of proportions of sulfate from sulfide oxidation (Y_{SO}), shallow groundwater (Y_{SG}) and HW01 (Y_{HW01}); (c–e) spatial fluctuation patterns of geothermal reservoir temperatures. Chal: chalcedony.

Table 3. Partial correlation relationships of geothermometers and secondary processes, and the extent to which the reservoir temperatures estimated for geothermal samples (except for HW01) deviate from those estimated for HW01.

| Methods | Geothermal Reservoir Temperature, T (°C) | | | Partial Correlation Coefficient | | | $\Delta T = (T - T_{HW01})/T_{HW01}$ (%) | |
|---|--|------|---|---------------------------------|-----------|------------|--|-------------------------------|
| | HW01 | HW09 | Average \pm SD ^a (n = 14) | Y_{SO} | Y_{SG} | Y_{HW01} | Max-Derivation | Average \pm SD ^b |
| Chalcedony [8] | 121 | 132 | 105 \pm 19 | −0.395 | −0.562 * | 0.383 | −36 | −14 \pm 15 (n = 13) |
| Chalcedony [64] | 118 | 129 | 104 \pm 18 | −0.395 | −0.562 * | 0.383 | −34 | −13 \pm 15 (n = 13) |
| Quartz [10] | 147 | 157 | 132 \pm 17 | −0.395 | −0.562 * | 0.383 | −27 | −11 \pm 11 (n = 13) |
| Quartz [8] | 146 | 157 | 132 \pm 17 | −0.396 | −0.562 * | 0.383 | −27 | −10 \pm 12 (n = 13) |
| Quartz [65] | 146 | 157 | 132 \pm 17 | −0.396 | −0.562 * | 0.383 | −27 | −10 \pm 12 (n = 13) |
| Na-K-Ca Mg corr [9] | 156 | 134 | 147 \pm 11 | −0.447 | −0.424 | 0.306 | −17 | −6 \pm 7 (n = 13) |
| K-Mg [13] | 126 | 109 | 115 \pm 8 | −0.730 *** | −0.652 ** | 0.437 | −18 | −9 \pm 6 (n = 13) |
| ¹⁸ O(SO ₄ -H ₂ O) [72] | 128 | 196 | 141 \pm 31 | 0.898 *** | −0.624 * | −0.725 ** | 53 | 11 \pm 24 (n = 10) |
| ¹⁸ O(SO ₄ -H ₂ O) [16] | 130 | 198 | 142 \pm 30 | 0.899 *** | −0.624 * | −0.730 ** | 52 | 10 \pm 24 (n = 10) |
| ¹⁸ O(SO ₄ -H ₂ O) [35] | 121 | 196 | 135 \pm 34 | 0.897 *** | −0.623 * | −0.718 ** | 62 | 13 \pm 28 (n = 10) |

Note(s): the significance levels are indicated: *** $p < 0.01$, ** $p < 0.05$, * $p < 0.1$. ^a The average geothermal reservoir temperatures with standard deviations (average \pm SD) of 14 geothermal water samples (Table S3). ^b The average values with standard deviations (average \pm SD) of 10–13 geothermal water samples, representing the extent to which the reservoir temperatures estimated for these geothermal samples (except for HW01) deviate from those estimated for HW01 ($\Delta T = (T - T_{HW01})/T_{HW01}$ (%)) (Table S4).

5.4.2. Geothermal Reservoir Temperature

Compared with classical geothermometers, which calculate the solubility of a few minerals or (semi-)empirical correlations, geothermometric modeling involves complete fluid analyses and a solid thermodynamic basis [7,73]. It is useful to identify equilibrated and nonequilibrated waters, especially to detect and eliminate mixing and CO₂ loss processes to reconstruct the existing equilibrium information. The geothermal reservoir in the study area is dominated by sandstone, consisting of quartz, plagioclase, K-feldspar, clay, calcite, anhydrite and dolomite (Table S5). Based on the lithology of the geothermal reservoir in the study area and in similar geothermal environments, an assemblage of eight minerals, including chalcedony, microcline, calcite, dolomite, kaolinite, Ca-montmorillonite, Mg-montmorillonite and anhydrite, were selected for thermodynamic simulation. Geothermometric modeling was conducted for samples HW01 and HW04, which are not significantly related to shallow processes of sulfate oxidation.

A Q/K graph for HW01 shows that different mineral curves scatter over a temperature range from 80 to 150 °C (Figure 9a). In addition, the supersaturation of calcite and dolomite at the sampling and chalcedony temperatures indicates that CO₂ degassing occurred. The dilution and CO₂ loss effects were eliminated by the addition of 0.0008 mol/L CO₂ and removal of 0.2 kg of water from the initial 1.0 kg of solvent water (Figure 9b), which changed the pH from the measured value of 6.78 to a computed value of 5.86. The reconstructed Q/K graph with good convergence reveals a reservoir temperature of 143 ± 4 °C, ranging from 135 to 149 °C. The same processes were also conducted on HW04, and a similar equilibrium temperature was achieved at 140 ± 5 °C in the range of 132–147 °C by the addition of 0.0015 mol/L CO₂ and removal of 0.35 kg of water from the initial 1.0 kg of solvent water (Figure 9c,d).

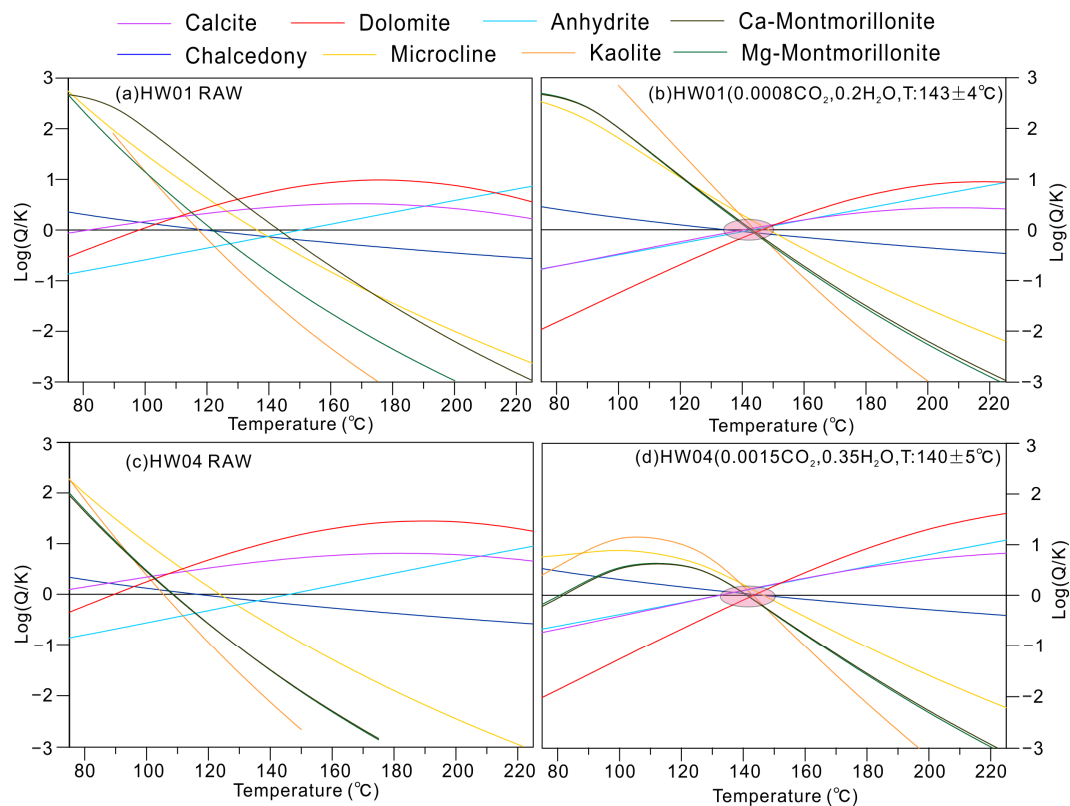


Figure 9. Influence of mixing and degassing on Q/K graphs for geothermal water from HW01 and HW04, (a,c) the original Q/K graphs (RAW); (b,d) the corrected Q/K graphs after the addition of water and CO₂.

The geothermal reservoir temperature of 142 ± 5 °C calculated by geothermometric modeling agrees well with the average temperature of 147 ± 11 °C calculated by the magnesium correction Na-K-Ca geothermometer. It is reasonable to infer that the geothermal reservoir temperature in the study area is 144 ± 8 °C on average. Accordingly, geothermal water circulates at depths of 3.6–4.6 km based on a geothermal gradient (G) of 29–37 °C/km, a constant temperature zone depth (Z_0) of 20 m and a normal temperature zone temperature (T_0) of 12.3 °C (Equation (11), [48,49]).

$$Z = Z_0 + (T_z - T_0)/G \quad (11)$$

where Z and Z_0 are the circulation depth of the water and the depth of the constant temperature zone, respectively (km); T_z and T_0 are the temperatures (°C) of the geothermal reservoir and the normal temperature zone, respectively; and G is the geothermal gradient (°C/km).

5.5. Conceptual Model of the Sulfur and Oxygen Isotope Evolution of Sulfate

The geothermal fluid evolution history and the conceptual model of the sulfur and oxygen isotope evolution of sulfate in Jimo geothermal water are shown in Figure 10. Paleometeoric water carrying sulfur-containing atmospheric deposits with high $\delta^{34}\text{S}_{\text{SO}_4}$ values infiltrates into the deep crust at depths of 3.6–4.6 km. The $\delta^{18}\text{O}_{\text{SO}_4}$ of dissolved sulfate is influenced by oxygen isotope exchange between sulfate and water at a geothermal reservoir temperature of 144 ± 8 °C. When deep geothermal fluids migrate from the deep reservoir to the surface and flow from the central parts to the eastern and western parts, geothermal water experiences sulfide oxidation and mixing of shallow groundwater. In the middle parts, the sulfate from sulfide oxidation and shallow groundwater mixing were less than 27% and 31% of the total SO_4 , respectively. In the eastern parts, 80–85% of the total SO_4 is derived from pyrite oxidation, which increases SO_4 concentrations and decreases $\delta^{34}\text{S}_{\text{SO}_4}$ and $\delta^{18}\text{O}_{\text{SO}_4}$ values. The low pH caused by pyrite oxidation further induces carbonate and silicate dissolution, introducing Ca, Mg, Al and Si into the geothermal water. In the western region, the increasing influence of shallow groundwater and relatively weaker oxidation of multimetal sulfides (e.g., ZnS, MnS, MnS_2 and MoS_2) cause slight increases in SO_4 , Mn, Zn and Mo concentrations and decreases in $\delta^{34}\text{S}_{\text{SO}_4}$ values and relatively constant $\delta^{18}\text{O}_{\text{SO}_4}$ values. The proportions of sulfate produced by multimetal sulfide oxidation range from 43 to 66%, with the contributions of shallow groundwater (23–47%) being greater than those of deep geothermal water (8–19%).

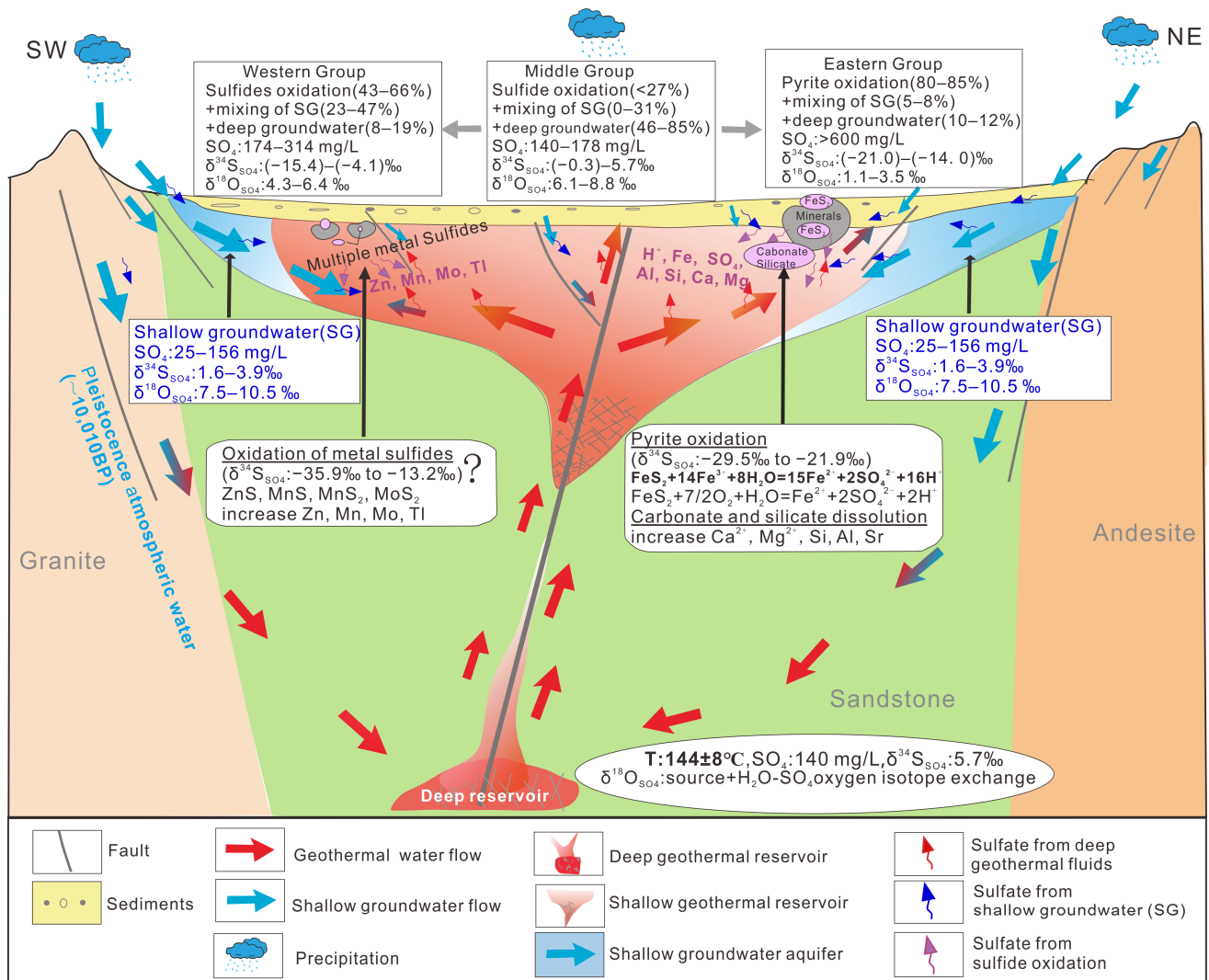


Figure 10. A conceptual model showing the evolution of geochemical characteristics and sulfur and oxygen isotope of sulfate in geothermal water.

6. Conclusions

This study quantifies the sulfate sources, processes controlling sulfur and oxygen isotopes of sulfate in Jimo geothermal waters and their influence on geothermometric estimates. The major findings are as follows:

The $\delta^{34}\text{S}_{\text{SO}_4}$ - $\delta^{18}\text{O}_{\text{SO}_4}$ - SO_4 - SO_4/Cl -trace element systematics suggest that SO_4^{2-} in the Middle Group geothermal waters primarily originates from atmospheric deposition, with sulfide oxidation contributing less than 27%. In contrast, in the Eastern and Western Groups, sulfide oxidation is the dominant sulfate source, accounting for 80–85% and 43–66% of SO_4^{2-} , respectively. Isotope mass balance calculations reveal distinct $\delta^{34}\text{S}$ values of sulfides between the two regions, with values ranging from -35.9‰ to -13.2‰ for multimetal sulfides in the west and from -29.5‰ to -21.9‰ for pyrite in the east.

Dramatic geochemical and isotopic variations are driven by oxygen isotope exchange between sulfate and water, sulfide oxidation and induced carbonate and silicate dissolution and mixing of shallow groundwater. These processes significantly affect geothermometric estimates, with sulfide oxidation leading to temperature overestimations of up to 52–62% by sulfate–water oxygen isotope geothermometers. The reliable geothermal reservoir temperature is estimated to be $144 \pm 8 \text{ °C}$.

Further research on geothermometer calibration to account for sulfide oxidation is essential for more accurate reservoir temperature estimates. In addition, deep drilling, direct reservoir temperature measurements and long-term chemical monitoring are needed to validate geothermometric estimates and assess renewability of geothermal water.

Supplementary Materials: The following supporting information can be downloaded at: <https://www.mdpi.com/article/10.3390/w17060788/s1>, Figure S1: Na-K-Mg geothermometer for geothermal waters; Table S1: Physical and chemical parameters and water isotopes in geothermal waters, shallow groundwater and seawater; Table S2. Temperature equations for the silica, cation and isotope geothermometers; Table S3: Synthesis of geothermal reservoir temperatures (°C) estimated by different geothermometers for the Jimo geothermal waters; Table S4: The extent to which the reservoir temperatures estimated for geothermal samples (except for HW01) deviate from those estimated for HW01; Table S5: The composition of mineral phases in sandstone.

Author Contributions: Conceptualization, Y.H., Z.P. and Q.G.; methodology, Y.H.; validation, Y.H. and Z.P.; formal analysis, Y.H.; investigation, Y.H. and D.L.; data curation, Y.H. and N.L.; writing—original draft preparation, Y.H.; writing—review and editing, Z.P., N.L., D.L., Q.G. and Z.L.; supervision, Z.P.; project administration, Z.L.; funding acquisition, Z.P. and Y.H. All authors have read and agreed to the published version of the manuscript.

Funding: This research was funded by the National Natural Science Foundation of China (Grant Nos. 42102292, 42130809), Key Laboratory of Synergetic Control and Joint Remediation for Soil & Water Pollution, Ministry of Ecology and Environment (GHBK-2023-02), GDAS Project of Science and Technology Development (2022GDASZH-2022010104) and Evaluation of Rare Earth Resources in Important Metallogenic Areas of Guangdong Province under the Geological Exploration and Urban Geology of Guangdong Province (2024-26).

Data Availability Statement: All data needed to evaluate the conclusions in the paper are present in the text and Supplementary Materials.

Conflicts of Interest: The authors declare no conflicts of interest.

References

1. Arnórsson, S.; D'Amore, F. *Isotopic and Chemical Techniques in Geothermal Exploration, Development and Use: Sampling Methods, Data Handling, Interpretation*; Arnórsson, S., Ed.; International Atomic Energy Agency: Vienna, Austria, 2000; pp. 152–212.
2. Wei, Z.; Huang, S.; Wang, C. Geochemistry and sources of boron and strontium of geothermal waters from the Pearl River Delta region, South China: Implications for water-rock interactions. *J. Geochem. Explor.* **2024**, *262*, 107492. [[CrossRef](#)]
3. Hao, Y.; Zhou, H.; Kuang, X.; Gong, Q.; Feng, Y.; Zhu, M.; Li, N.; Shi, X. Lithium isotopes in the geothermal waters of the India–Asia continental convergent margin: Source and evolution. *Geosci. Front.* **2025**, *16*, 102001. [[CrossRef](#)]
4. Jolie, E.; Scott, S.; Faulds, J.; Isabelle Chambefort, I.; Axelsson, G.; Gutiérrez-Negrín, L.C.; Regenspurg, S.; Ziegler, M.; Ayling, B.; Richter, A.; et al. Geological controls on geothermal resources for power generation. *Nat. Rev. Earth Env.* **2021**, *2*, 324–339. [[CrossRef](#)]
5. Halas, S.; Trembaczowski, A.; Soltyk, W.; Walendziak, J. Sulphur and Oxygen Isotopes in Sulphates in Natural Waters: (2) Deep-Waters from Horizons Below Baltic Sea Floor. *Isot. Environ. Health Stud.* **1993**, *28*, 229–235. [[CrossRef](#)]
6. Boschetti, T. Oxygen isotope equilibrium in sulfate–water systems: A revision of geothermometric applications in low-enthalpy systems. *J. Geochem. Explor.* **2013**, *124*, 92–100. [[CrossRef](#)]
7. Spycher, N.; Peiffer, L.; Sonnenthal, E.L.; Saldi, G.; Reed, M.H.; Kennedy, B.M. Integrated multicomponent solute geothermometry. *Geothermics* **2014**, *51*, 113–123. [[CrossRef](#)]
8. Fournier, R.O. Chemical geothermometers and mixing models for geothermal systems. *Geothermics* **1977**, *5*, 41–50. [[CrossRef](#)]
9. Fournier, R.O.; Potter, R.W. Magnesium correction to the Na-K-Ca chemical geothermometer. *Geochim. Cosmochim. Acta* **1979**, *43*, 1543–1550. [[CrossRef](#)]
10. Fournier, R.O.; Potter, R.W. An equation correlating the solubility of quartz in water from 25 to 900 °C at pressures up to 10,000 bars. *Geochim. Cosmochim. Acta* **1982**, *46*, 1975–1978. [[CrossRef](#)]
11. Fournier, R.O. A revised equation for the Na/K geothermometer. *Geotherm. Res. Counc. Trans.* **1979**, *3*, 221–224.
12. Arnórsson, S. *Interpretation of Chemical and Isotopic Data on Fluids Discharged from Wells in the Momotombo Geothermal Field with Notes on Gas Chromatography Analysis*; Project NIC/8/008-05; IAEA Report: Seoul, Republic of Korea, 1998; 28p.

13. Giggenbach, W.F. Geothermal solute equilibria. Derivation of Na–K–Mg–Ca geoindicators. *Geochim. Cosmochim. Acta* **1988**, *52*, 2749–2765. [[CrossRef](#)]
14. Fournier, R.O.; Truesdell, A.H. An empirical Na–K–Ca geothermometer for natural waters. *Geochim. Cosmochim. Acta* **1973**, *37*, 1255–1275. [[CrossRef](#)]
15. Kharaka, Y.K.; Lico, M.S.; Law, L.M. Chemical geothermometers applied to formation waters, Gulf of Mexico and California Basins (abstract). *Am. Ass. Petrol. Geol. Bull.* **1982**, *66*, 588.
16. Lloyd, R.M. Oxygen isotope behavior in the sulfate-water system. *J. Geophys. Res.* **1968**, *73*, 6099. [[CrossRef](#)]
17. Pang, Z.H.; Reed, M. Theoretical chemical thermometry on geothermal waters: Problems and methods. *Geochim. Cosmochim. Acta* **1998**, *62*, 1083–1091. [[CrossRef](#)]
18. Sanjuan, B.; Millot, R.; Ásmundsson, R.; Brach, M.; Giroud, N. Use of two new Na/Li geothermometric relationships for geothermal fluids in volcanic environments. *Chem. Geol.* **2014**, *389*, 60–81. [[CrossRef](#)]
19. Pang, Z.H.; Yang, F.T.; Luo, L. Determination method of reservoir temperature in geothermal field. In *Solid Earth Science Research Methods*; Zhongli, D., Ed.; Science Press: Beijing, China, 2013; pp. 219–242.
20. Ferguson, G.; Grasby, S.E.; Hindle, S.R. What do aqueous geothermometers really tell us? *Geofluids* **2009**, *9*, 39–48. [[CrossRef](#)]
21. Serpen, U. Hydrogeological investigations on Balcoea geothermal system in Turkey. *Geothermics* **2004**, *33*, 309–335. [[CrossRef](#)]
22. Liao, Z. *Thermal Springs and Geothermal Energy in the Qinghai-Tibetan Plateau and the Surroundings*; Springer Hydrogeology; Springer: Singapore, 2018; 311p.
23. Hao, Y.; Pang, Z.; Kong, Y.; Tian, J.; Wang, Y.; Liao, D.; Fan, Y. Chemical and isotopic constraints on the origin of saline waters from a hot spring in the eastern coastal area of China. *Hydrogeol. J.* **2020**, *28*, 2457–2475. [[CrossRef](#)]
24. Zheng, T.; Stefánsson, A.; Kang, F.; Shi, M.; Jiang, H.; Sui, H. Geochemical and isotope constraints on the hydrogeology and geochemistry of the geothermal waters in the Shandong Peninsula, China. *Geothermics* **2023**, *108*, 102628. [[CrossRef](#)]
25. Stefánsson, A.; Keller, N.S.; Robin, J.G.; Ono, S. Multiple sulfur isotope systematics of Icelandic geothermal fluids and the source and reactions of sulfur in volcanic geothermal systems at divergent plate boundaries. *Geochim. Cosmochim. Acta* **2015**, *165*, 307–323. [[CrossRef](#)]
26. Bao, Y.; Pang, Z.; Huang, T.; Li, Y.; Tian, J.; Luo, J.; Qian, T. Chemical and isotopic evidences on evaporite dissolution as the origin of high sulfate water in a karst geothermal reservoir. *Appl. Geochem.* **2022**, *145*, 105419. [[CrossRef](#)]
27. Li, B.; Kong, Q.; Liao, F.; Wang, G.; Liu, F.; Guo, L.; Liu, C.; Shi, Z. Sulphur evolution in acidic and alkaline geothermal water related to magma in the Rehai geothermal field in the southeastern Tibet Plateau based on stable hydrogen, oxygen, sulphur isotopes. *Geothermics* **2024**, *119*, 102931. [[CrossRef](#)]
28. Krouse, H.R.; Mayer, B. Sulfur and oxygen isotopes in sulfate. In *Environmental Tracers in Subsurface Hydrology*; Cook, P.G., Herczeg, A.L., Eds.; Kluwer: Boston, MA, USA, 2000; Chapter 7; pp. 195–231.
29. Seal, R.R., II. Sulfur Isotope Geochemistry of Sulfide Minerals. *Rev. Min. Geochem.* **2006**, *61*, 633–677. [[CrossRef](#)]
30. Marini, L.; Moretti, R.; Accornero, M. Sulfur isotopes in magmatic-hydrothermal systems, melts, and magmas. *Rev. Min. Geochem.* **2011**, *73*, 423–492. [[CrossRef](#)]
31. Taylor, B.E.; Wheeler, M.C. Sulfur- and oxygen-isotope geochemistry of acid mine drainage in the western US: Field and experimental studies revisited. In *Environmental Geochemistry of Sulfide Oxidation*; Alpers, C.N., Blowes, D.W., Eds.; ACS Symposium Series 550; American Chemical Society: Washington, DC, USA, 1994; pp. 481–514.
32. Balci, N.; Mayer, B.; Shanks, W.; Mandernack, K. Oxygen and sulfur isotope systematics of sulfate produced during abiotic and bacterial oxidation of sphalerite and elemental sulfur. *Geochem. Cosmochim. Acta* **2012**, *77*, 335–351. [[CrossRef](#)]
33. Hosono, T.; Lorphensriand, O.; Onodera, S.; Okawa, H.; Nakano, T.; Yamanaka, T.; Tsujimura, M.; Taniguchi, M. Different isotopic evolutionary trends of $\delta^{34}\text{S}$ and $\delta^{18}\text{O}$ compositions of dissolved sulfate in an anaerobic deltaic aquifer system. *Appl. Geochem.* **2014**, *46*, 30–42. [[CrossRef](#)]
34. Long, Y.; Huang, T.; Zhang, F.; Li, Z.; Pang, Z. Origin of sulfate in the unsaturated zone and groundwater of a loess aquifer. *Hydrol. Process.* **2021**, *35*, e14166. [[CrossRef](#)]
35. Mizutani, Y.; Rafter, T.A. Oxygen isotopic composition of sulphates—Part 4. *N. Z. J. Sci.* **1969**, *12*, 60–68.
36. Zhang, D.; Li, X.; Zhao, Z.; Liu, C. Using dual isotopic data to track the sources and behaviors of dissolved sulfate in the western North China Plain. *Appl. Geochem.* **2015**, *52*, 43–56. [[CrossRef](#)]
37. Li, L.; Wei, S.; Sherwood Lollar, B.; Wing, B.; Bui, T.H.; Ono, S.; Lau Vetter, M.C.Y.; Onstott, T.C.; Kieft, T.L.; Borgonie, G.; et al. In situ oxidation of sulfide minerals supports widespread sulfate reducing bacteria in the deep subsurface of the Witwatersrand Basin (South Africa): Insights from multiple sulfur and oxygen isotopes. *Earth Planet. Sci. Lett.* **2022**, *577*, 117247. [[CrossRef](#)]
38. Zeebe, R.E. A new value for the stable oxygen isotope fractionation between dissolved sulfate ion and water. *Geochim. Cosmochim. Acta* **2010**, *74*, 818–828. [[CrossRef](#)]
39. Zhang, T.; Zhang, Y.Q. Late Mesozoic tectono-magmatic evolution history of the Jiaobei Uplift, Shandong Peninsula. *Acta Geol. Sin.* **2008**, *82*, 1210–1218, (In Chinese with English abstract)

40. Liu, Y.; Fu, Y.; Wu, S. δD and $\delta^{18}O$ compositions in geothermal water of Jimo hot spring and its geological significance. *Coast. Eng.* **2009**, *28*, 52–60, (In Chinese with English abstract).
41. Zhang, L.; Wang, C.; Cao, K.; Wang, Q.; Tan, J. High elevation of Jiaolai Basin during the Late Cretaceous: Implication for the coastal mountains along the East Asian margin. *Earth Planet. Sci. Lett.* **2016**, *456*, 112–113. [[CrossRef](#)]
42. Ji, Q. On the Cretaceous stratigraphic framework and the Cretaceous-Paleogene boundary of Eastern Shandong Province. *J. Geol.* **2017**, *4*, 1–25, (In Chinese with English abstract).
43. Hao, Y.; Pang, Z.; Tian, J.; Wang, Y.; Li, Z.; Li, L.; Xing, L. Origin and evolution of hydrogen-rich gas discharges from a hot spring in the eastern coastal area of China. *Chem. Geol.* **2020**, *538*, 119477. [[CrossRef](#)]
44. Liu, Y.; Cao, X.; Fu, Y.; Wu, S. Dynamic change characteristics of geothermal water quality in Jimo Hot Springs. *Land. Resour. Shandong Prov.* **2010**, *26*, 19–24.
45. Fang, B. Perspective Prognosis on Geothermal Resource in Synthetic Information in Shandong Province. Ph.D. Thesis, Jilin University, Changchun, China, 2006.
46. Jiang, G.; Hu, S.; Shi, Y.; Zhang, C.; Wang, Z.; Hu, D. Terrestrial heat flow of continental China: Updated dataset and tectonic implications. *Tectonophysics* **2019**, *753*, 36–48. [[CrossRef](#)]
47. Torres-Martínez, J.A.; Mora, A.; Knappett, P.S.K.; Ornelas-Soto, N.; Mahlkecht, J. Tracking nitrate and sulfate sources in groundwater of an urbanized valley using a multi-tracer approach combined with a Bayesian isotope mixing model. *Water Res.* **2020**, *182*, 115962. [[CrossRef](#)]
48. Reed, M.; Spycher, N. Calculation of pH and mineral equilibria in hydrothermal waters with application to geothermometry and studies of boiling and dilution. *Geochim. Cosmochim. Acta* **1984**, *48*, 1479–1492. [[CrossRef](#)]
49. Reed, M.; Spycher, N.; Palandri, J. *Manual of SOLVEQ-XPT: A Computer Program for Computing Aqueous-Mineral-Gas Equilibria*; Lawrence Berkeley Laboratory, Department of Energy: Berkeley, CA, USA, 2010; 41p.
50. Peters, C.; Strauss, H.; Haase, K.; Bach, W.; de Ronde, C.E.J.; Kleint, C.; Stucker, V.; Diehl, A. SO_2 disproportionation impacting hydrothermal sulfur cycling: Insights from multiple sulfur isotopes for hydrothermal fluids from the Tonga-Kermadec intraoceanic arc and the NE Lau Basin. *Chem. Geol.* **2021**, *586*, 120586. [[CrossRef](#)]
51. Rees, C.E.; Jenkins, W.J.; Monster, J. The sulphur isotope geochemistry of ocean water sulphate. *Geochim. Cosmochim. Acta* **1978**, *42*, 377–382. [[CrossRef](#)]
52. Nriagu, J.O.; Ress, C.E.; Mekhtiyeva, V.L.; Lein, A.Y.; Fritz, P.; Drimmie, R.J.; Pankina, R.G.; Robinson, R.W.; Krouse, H.R. Hydrosphere. In *Stable Isotopes in the Assessment of Natural and Anthropogenic Sulphur in the Environment*; Krouse, H.R., Grinenko, V.A., Eds.; SCOPE 43; John and Wiley and Sons: Hoboken, NJ, USA, 1991; pp. 177–265.
53. Claypool, G.E.; Holser, W.T.; Kaplan, I.R.; Sakai, H.; Zak, I. The age curves of sulfur and oxygen isotopes in marine sulfate and their mutual interpretation. *Chem. Geol.* **1980**, *28*, 199–260. [[CrossRef](#)]
54. Bojar, A.-V.; Halas, S.; Bojar, H.-P.; Trembaczowski, A. Late Permian to Triassic isotope composition of sulfates in the Eastern Alps: Palaeogeographic implications. *Geol. Mag.* **2018**, *155*, 797–810. [[CrossRef](#)]
55. González-Partida, E.; Carrillo-Chávez, A.; Levresse, G.; Tello-Hinojosa, E.; Venegas-Salgado, S.; Ramirez-Silva, G.; Pal-Verma, M.; Tritlla, J.; Camprubi, A. Hydrogeochemical and isotopic fluid evolution of the Los Azufres geothermal field, Central Mexico. *Appl. Geochem.* **2005**, *20*, 23–39. [[CrossRef](#)]
56. Martínez Serrano, R.G.; Jacquier, B.; Arnold, M. The $\delta^{34}S$ composition of sulfates and sulfides at the Los Humeros geothermal system, Mexico and their application to physicochemical fluid evolution. *J. Volcanol. Geotherm. Res.* **1996**, *73*, 99–118. [[CrossRef](#)]
57. Taylor, B.E.; Wheeler, M.C.; Nordstrom, D.K. Stable isotope geochemistry of acid mine drainage: Experimental oxidation of pyrite. *Geochim. Cosmochim. Acta* **1984**, *48*, 2669. [[CrossRef](#)]
58. Gilhooly, W.P., III; Reinhard, C.T.; Lyons, T.W. A comprehensive sulfur and oxygen isotope study of sulfur cycling in a shallow, hyper-euxinic meromictic lake. *Geochim. Cosmochim. Acta* **2016**, *189*, 1–23. [[CrossRef](#)]
59. Toran, L.; Harris, R.F. Interpretation of sulfur and oxygen isotopes in biological and abiological sulfide oxidation. *Geochim. Cosmochim. Acta* **1989**, *53*, 2341–2348. [[CrossRef](#)]
60. Dogramaci, S.; McLean, L.; Skrzypek, G. Hydrochemical and stable isotope indicators of pyrite oxidation in carbonate-rich environment; the Hamersley Basin, Western Australia. *J. Hydrol.* **2017**, *545*, 288–298. [[CrossRef](#)]
61. Migaszewski, Z.M.; Gałuszka, A.; Dołęgowska, S. Stable isotope geochemistry of acid mine drainage from the Wiśniówka area (south-central Poland). *Appl. Geochem.* **2018**, *95*, 45–56. [[CrossRef](#)]
62. Van Everingden, R.O.; Krouse, H.R. Isotope composition of sulphates generated by bacterial and abiological oxidation. *Nature* **1985**, *315*, 395–396. [[CrossRef](#)]
63. Tuttle, M.L.W.; Breit, G.N.; Cozzarelli, I.M. Processes affecting $\delta^{34}S$ and $\delta^{18}O$ values of dissolved sulfate in alluvium along the Canadian River, central Oklahoma, USA. *Chem. Geol.* **2009**, *265*, 455–467. [[CrossRef](#)]
64. Arnórsson, S.; Gunnlaugsson, E.; Svavarsson, H. The chemistry of geothermal waters in Iceland.3. Chemical geothermometry in geothermal investigations. *Geochim. Cosmochim. Acta* **1983**, *47*, 567–577. [[CrossRef](#)]

65. Truesdell, A.H. Summary of section III. Geochemical techniques in exploration. In Proceedings of the Second United States Symposium on the Development and Use of Geothermal Resources, San Francisco, CA, USA, 20–29 May 1975; US Government Printing Office: Washington, DC, USA, 1976; pp. 53–79.
66. Tonani, F. Some remarks on the application of geochemical techniques in geothermal exploration. In *Advances in European Geothermal Research*; Springer: Dordrecht, The Netherlands, 1980; pp. 428–443.
67. Nieva, D.; Nieva, R. Developments in geothermal energy in Mexico, Part 12. A cationic geothermometer for prospecting of geothermal resources. *Heat Recovery Syst. CHP* **1987**, *7*, 243–258. [[CrossRef](#)]
68. Can, I. A new improved Na/K geothermometer by artificial neural networks. *Geothermics* **2002**, *31*, 751–760. [[CrossRef](#)]
69. Fouillac, C.; Micard, G. Sodium/Lithium ratios in water applied to geothermometry of geothermal reservoirs. *Geothermics* **1981**, *10*, 55–70. [[CrossRef](#)]
70. Verma, S.P.; Santoyo, E. New improved equations for Na/K, Na/Li and SiO₂ geothermometers by outlier detection and rejection. *J. Volcanol. Geotherm. Res.* **1997**, *79*, 9–23. [[CrossRef](#)]
71. Kharaka, Y.K.; Mariner, R.H. Chemical Geothermometers and Their Application to Formation Waters from Sedimentary Basins. In *Thermal History of Sedimentary Basins*; Naeser, N.D., McCulloh, T.H., Eds.; Springer: New York, NY, USA, 1989; pp. 99–117.
72. Seal, R.R., II; Rye, R.O.; Alpers, C.N. Stable isotope systematics of sulfate minerals. *Rev. Miner. Geochem.* **2000**, *40*, 541–602. [[CrossRef](#)]
73. Peiffer, L.; Wanner, C.; Spycher, N.; Sonnenthal, E.; Kennedy, B.M. Multicomponent vs. classical geothermometry: An evaluation using reactive transport modeling. *Procedia Earth Planet. Sci.* **2013**, *7*, 665–668. [[CrossRef](#)]

Disclaimer/Publisher’s Note: The statements, opinions and data contained in all publications are solely those of the individual author(s) and contributor(s) and not of MDPI and/or the editor(s). MDPI and/or the editor(s) disclaim responsibility for any injury to people or property resulting from any ideas, methods, instructions or products referred to in the content.